

# Plug-and-Play Algorithms for Large-scale Snapshot Compressive Imaging

Xin Yuan  
Bell Labs  
NJ USA

xyuan@bell-labs.com

Yang Liu  
MIT  
MA USA

yliu12@mit.edu

Jinli Suo      Qionghai Dai  
Dept. of Automation & Institute for Brain and  
Cognitive Sciences, Tsinghua Univ., Beijing China

{jlsuo, daigh}@tsinghua.edu.cn

## Abstract

*Snapshot compressive imaging (SCI) aims to capture the high-dimensional (usually 3D) images using a 2D sensor (detector) in a single snapshot. Though enjoying the advantages of low-bandwidth, low-power and low-cost, applying SCI to large-scale problems (HD or UHD videos) in our daily life is still challenging. The bottleneck lies in the reconstruction algorithms; they are either too slow (iterative optimization algorithms) or not flexible to the encoding process (deep learning based end-to-end networks). In this paper, we develop fast and flexible algorithms for SCI based on the plug-and-play (PnP) framework. In addition to the widely used PnP-ADMM method, we further propose the PnP-GAP (generalized alternating projection) algorithm with a lower computational workload and prove the global convergence of PnP-GAP under the SCI hardware constraints. By employing deep denoising priors, we first time show that PnP can recover a UHD color video ( $3840 \times 1644 \times 48$  with PNSR above 30dB) from a snapshot 2D measurement. Extensive results on both simulation and real datasets verify the superiority of our proposed algorithm. The code is available at <https://github.com/liuyang12/PnP-SCI>.*

## 1. Introduction

Computational imaging [1, 31] constructively combines optics, electronics and algorithms for optimized performance [4, 6, 32] or to provide new abilities [5, 25, 35, 43] to imaging systems. One important branch of computational imaging with promising applications is snapshot compressive imaging (SCI) [23, 45], which utilized a two-dimensional (2D) camera to capture 3D video or spectral data. Different from conventional cameras, such imaging systems adopt sampling on a set of consecutive images—video frames (e.g., CACTI [23, 61]) or spectral channels (e.g., CASSI [46])—in accordance with the sensing matrix and integrating these sampled signals along time or spectrum to obtain the final compressed measurements. With this technique, SCI systems [12, 15, 36, 42, 45, 46, 61] can

capture the high-speed motion [40, 41, 62, 63, 69, 71] and high-resolution spectral information [28, 70, 37] but with low memory, low bandwidth, low power and potentially low cost. In this work, we focus on video SCI reconstruction.

In parallel to the hardware development, various algorithms have been employed and developed for SCI reconstruction. In addition to the widely used TwIST [2], Gaussian Mixture Model (GMM) in [49, 50] based algorithms model the pixels within a spatial-temporal patch by a GMM. GAP-TV [53] adopts the idea of total variance minimization under the generalized alternating projection (GAP) [21] framework. Most recently, DeSCI proposed in [22] has led to state-of-the-art results. However, the slow speed of DeSCI precludes its real applications, especially to the HD ( $1280 \times 720$ ), FHD ( $1920 \times 1080$ ) or UHD ( $3840 \times 1644$  in Fig. 1 and  $3840 \times 2160$  in Fig. 5) videos, which are getting popular in our daily life. Recall that DeSCI needs more than one hour to reconstruct a  $256 \times 256 \times 8$  video from a snapshot measurement. GAP-TV, by contrast, as a fast algorithm, cannot provide good reconstruction to be used in real applications (in general, this needs the  $\text{PSNR} \geq 30\text{dB}$ ). An alternative solution is to train an end-to-end network [26, 34] to reconstruct the videos for the SCI system. On one hand, this approach can finish the task within seconds and by appropriate design of multiple GPUs, an end-to-end sampling and reconstruction framework can be built. On the other hand, this method loses the *robustness* of the network since whenever the sensing matrix (encoding process) changes, a new network has to be re-trained. Moreover, it cannot be readily used in adaptive sensing [71].

Therefore, it is desirable to devise an *efficient* and *flexible* algorithm for SCI reconstruction, especially for large-scale problems. This will pave the way of applying SCI in our daily life [55]. In order to solve the *trilemma of speed, accuracy and flexibility* for SCI reconstruction, this paper makes the following contributions:

- Inspired by the plug-and-play (PnP) alternating direction method of multiplier (ADMM) [9] framework, we extend PnP-ADMM to SCI and show that PnP-ADMM converges to a *fixed point* by considering the hardware constraints

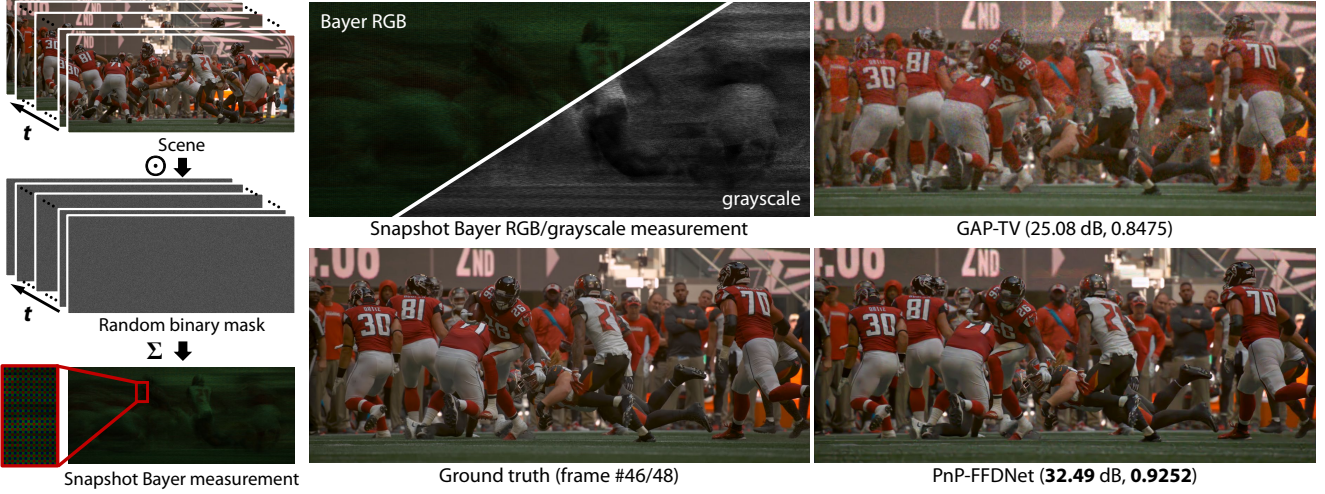


Figure 1. Sensing process of video SCI (left) and the reconstruction results using the proposed PnP-FFDNet (bottom-right). The captured image (middle-top) size is **UHD ( $3840 \times 1644$ )** and **48 frames** are recovered from a **snapshot measurement**. GAP-TV (top-right) takes 180 mins and PnP-FFDNet takes 55 mins for the reconstruction. All other methods are too slow (more than 12 hours) to be used.

and the special structure of the sensing matrix [18] in SCI.

- We propose an efficient PnP-GAP algorithm by using various *bounded denoisers* (Fig. 2) into the GAP [21], which has a lower computational workload than PnP-ADMM. In addition to the fixed point convergence, we further prove that, under proper assumptions, the solution of PnP-GAP will converge to the true signal. To our best knowledge, this is the first *global* convergence results for SCI and this also holds under the additive white Gaussian noise.
- By integrating the deep image denoiser, *e.g.*, the *fast and flexible* FFDNet [75] into PnP-GAP, we show that a FHD video ( $1920 \times 1080 \times 24$ ) can be recovered from a snapshot measurement (Fig. 5) within 2 minutes with PSNR close to 30dB using a single GPU plus a normal computer. Compared with an end-to-end network [26], dramatic resources have been saved (no re-training is required). This further makes the UHD compression using SCI to be feasible (a  $3840 \times 1644 \times 48$  video is reconstructed with PSNR above 30dB in Fig. 1). To our best knowledge, this is the first time that SCI is used in these large-scale problems.
- We apply our developed PnP algorithms to extensive simulation and real datasets (captured by real SCI cameras) to verify the efficiency and robustness of our proposed algorithms. We show that the proposed algorithm can obtain results on-par with DeSCI but with a significant reduction of computational time.

The rest of this paper is organized as follows. Sec. 2 reviews the mathematical model of video SCI. Sec. 3 develops the PnP-ADMM under the SCI hardware constraints and shows that PnP-ADMM converges to a fixed point. Sec. 4 develops the PnP-GAP algorithm and proves its global convergence. Sec. 5 integrates various denoisers into the PnP framework for SCI reconstruction. Extensive results of both (benchmark and large-scale) simulation and real data are

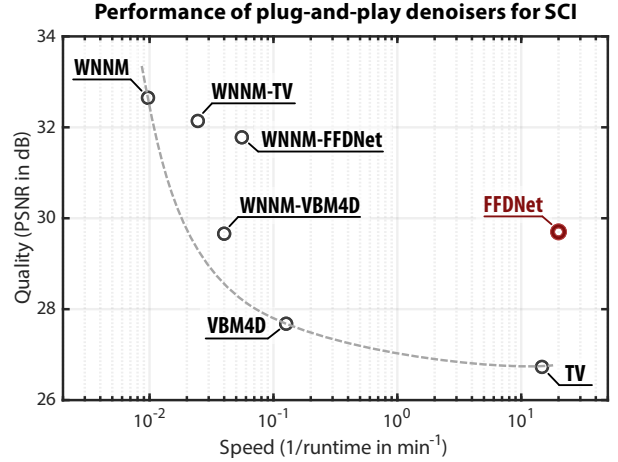


Figure 2. Trade-off of quality and speed of various plug-and-play denoising algorithms for SCI reconstruction.

presented in Sec. 6 and Sec. 7 concludes the paper.

**Related Work** SCI systems have been developed to capture 3D spectral images [8, 37, 70], videos [15, 33, 23, 25, 36, 40, 41, 43, 61, 68], high dynamic range [52], depth [24, 59, 67] and polarization [44] images, *etc.* From the algorithm side, in addition to sparsity [56, 66, 58, 60, 64, 54, 76, 72, 73] based algorithms, GMM [49, 50, 57] and GAP-TV [53] have been proposed. As mentioned above, DeSCI [22] has led to state-of-the-art results. Inspired by deep learning on image restoration [74], researchers have started using deep learning in computational imaging [16, 19, 20, 30, 39, 29, 65]. Some networks have been proposed for SCI reconstruction [26, 28, 34, 51]. Different from these methods, in this work, we integrate various denoisers into PnP framework [9, 38] for SCI reconstruction, thus to provide *efficient* and *flexible* algorithms for SCI. Our PnP algorithms can not only provide excellent results but also are robust to different

coding process and thus can be used in adaptive sensing.

## 2. Mathematical Model of SCI

As depicted in Fig. 1, in the video SCI system (e.g., CACTI) [23], consider that a  $B$ -frame video  $\mathbf{X} \in \mathbb{R}^{n_x \times n_y \times B}$  is modulated and compressed by  $B$  sensing matrices (masks)  $\mathbf{C} \in \mathbb{R}^{n_x \times n_y \times B}$ , and the measurement frame  $\mathbf{Y} \in \mathbb{R}^{n_x \times n_y}$  can be expressed as [23, 61]

$$\mathbf{Y} = \sum_{b=1}^B \mathbf{C}_b \odot \mathbf{X}_b + \mathbf{Z}, \quad (1)$$

where  $\mathbf{Z} \in \mathbb{R}^{n_x \times n_y}$  denotes the noise;  $\mathbf{C}_b = \mathbf{C}(:, :, b)$  and  $\mathbf{X}_b = \mathbf{X}(:, :, b) \in \mathbb{R}^{n_x \times n_y}$  represent the  $b$ -th sensing matrix (mask) and the corresponding video frame, respectively;  $\odot$  denotes the Hadamard (element-wise) product. Mathematically, the measurement in (1) can be expressed by

$$\mathbf{y} = \mathbf{H}\mathbf{x} + \mathbf{z}, \quad (2)$$

where  $\mathbf{y} = \text{Vec}(\mathbf{Y}) \in \mathbb{R}^{n_x n_y}$  and  $\mathbf{z} = \text{Vec}(\mathbf{Z}) \in \mathbb{R}^{n_x n_y}$ . Correspondingly, the video signal  $\mathbf{x} \in \mathbb{R}^{n_x n_y B}$  is

$$\mathbf{x} = \text{Vec}(\mathbf{X}) = [\text{Vec}(\mathbf{X}_1)^\top, \dots, \text{Vec}(\mathbf{X}_B)^\top]^\top. \quad (3)$$

Unlike traditional compressive sensing [7, 11], the sensing matrix  $\mathbf{H} \in \mathbb{R}^{n_x n_y \times n_x n_y B}$  in video SCI is sparse and is a concatenation of diagonal matrices

$$\mathbf{H} = [\mathbf{D}_1, \dots, \mathbf{D}_B]. \quad (4)$$

where  $\mathbf{D}_b = \text{diag}(\text{Vec}(\mathbf{C}_b)) \in \mathbb{R}^{n \times n}$  with  $n = n_x n_y$ , for  $b = 1, \dots, B$ . Consequently, the *sampling rate* here is equal to  $1/B$ . It has been proved recently in [17, 18] that the reconstruction error of SCI is bounded even when  $B > 1$ .

In the color video case, as shown in Figs. 1, 5 and 7, the raw data captured by the generally used Bayer pattern sensors have ‘‘RGGB’’ channels. Since the mask is imposed on each pixel, the generated measurement can be treated as a grayscale image as in Fig. 6 and when it is shown in color, the demosaicing procedure cannot generate the right color due to mask modulation (Fig. 5). Therefore, during reconstruction, we first recover each of these four channels independently and then perform demosaicing in the reconstructed videos. The final demosaiced RGB video is the desired signal [61].

## 3. Plug-and-Play ADMM for SCI

The inversion problem of SCI can be modeled as

$$\hat{\mathbf{x}} = \underset{\mathbf{x}}{\text{argmin}} f(\mathbf{x}) + \lambda g(\mathbf{x}), \quad (5)$$

where  $f(\mathbf{x})$  can be seen as the loss of the forward imaging model, i.e.,  $\|\mathbf{y} - \mathbf{H}\mathbf{x}\|_2^2$  and  $g(\mathbf{x})$  is a prior being used. This prior is usually playing the role of a regularizer.

### 3.1. Review the Plug-and-Play ADMM in [9]

Via using the ADMM framework [3], by introducing an auxiliary parameter  $\mathbf{v}$ , the unconstrained optimization in Eq. (5) can be converted into

$$(\hat{\mathbf{x}}, \hat{\mathbf{v}}) = \underset{\mathbf{x}, \mathbf{v}}{\text{argmin}} f(\mathbf{x}) + \lambda g(\mathbf{v}), \text{ subject to } \mathbf{x} = \mathbf{v}. \quad (6)$$

This minimization can be solved by the following sequence of sub-problems

$$\mathbf{x}^{(k+1)} = \underset{\mathbf{x}}{\text{argmin}} f(\mathbf{x}) + \frac{\rho}{2} \|\mathbf{x} - (\mathbf{v}^{(k)} - \frac{1}{\rho} \mathbf{u}^{(k)})\|_2^2, \quad (7)$$

$$\mathbf{v}^{(k+1)} = \underset{\mathbf{v}}{\text{argmin}} \lambda g(\mathbf{v}) + \frac{\rho}{2} \|\mathbf{v} - (\mathbf{x}^{(k)} + \frac{1}{\rho} \mathbf{u}^{(k)})\|_2^2, \quad (8)$$

$$\mathbf{u}^{(k+1)} = \mathbf{u}^{(k)} + \rho(\mathbf{x}^{(k+1)} - \mathbf{v}^{(k+1)}), \quad (9)$$

where the superscript  $^{(k)}$  denotes the iteration number.

While in SCI and other inversion problems,  $f(\mathbf{x})$  is usually a quadratic form and there are various solutions to Eq. (7). In PnP-ADMM, the solution of Eq. (8) is replaced by an off-the-shelf denoising algorithm, to yield

$$\mathbf{v}^{(k+1)} = \mathcal{D}_\sigma(\mathbf{x}^{(k)} + \frac{1}{\rho} \mathbf{u}^{(k)}). \quad (10)$$

where  $\mathcal{D}_\sigma$  denotes the denoiser being used with  $\sigma$  being the standard deviation of the assumed additive white Gaussian noise. In [9], the authors proposed to update the  $\rho$  in each iteration by  $\rho_{k+1} = \gamma_k \rho_k$  with  $\gamma_k \geq 1$  and setting  $\sigma_k = \sqrt{\lambda/\rho_k}$  for the denoiser. In this manner, the author defined the *bounded denoiser* and proved the *fixed point* convergence of the PnP-ADMM.

**Definition 1.** (*Bounded Denoiser* [9]): A bounded denoiser with a parameter  $\sigma$  is a function  $\mathcal{D}_\sigma : \mathbb{R}^n \rightarrow \mathbb{R}^n$  such that for any input  $\mathbf{x} \in \mathbb{R}^n$ ,

$$\frac{1}{n} \|\mathcal{D}_\sigma(\mathbf{x}) - \mathbf{x}\|_2^2 \leq \sigma^2 C, \quad (11)$$

for some universal constant  $C$  independent of  $n$  and  $\sigma$ .

With this definition (constraint on the denoiser) and the assumption of  $f : [0, 1]^n \rightarrow \mathbb{R}$  having bounded gradient, which is for any  $\mathbf{x} \in [0, 1]^n$ , there exists  $L < \infty$  such that  $\|\nabla f(\mathbf{x})\|_2 / \sqrt{n} \leq L$ , the authors of [9] have proved that: the iterates of the PnP-ADMM demonstrates a fixed-point convergence. That is, there exists  $(\mathbf{x}^*, \mathbf{v}^*, \mathbf{u}^*)$  such that  $\|\mathbf{x}^{(k)} - \mathbf{x}^*\|_2 \rightarrow 0$ ,  $\|\mathbf{v}^{(k)} - \mathbf{v}^*\|_2 \rightarrow 0$ , and  $\|\mathbf{u}^{(k)} - \mathbf{u}^*\|_2 \rightarrow 0$  as  $k \rightarrow \infty$ .

### 3.2. PnP-ADMM for SCI

In SCI, with the model stated in Eq. (2),  $\mathbf{x} \in \mathbb{R}^{nB}$ , and we consider the loss function  $f(\mathbf{x})$  as

$$f(\mathbf{x}) = \frac{1}{2} \|\mathbf{y} - \mathbf{H}\mathbf{x}\|_2^2. \quad (12)$$

Consider all the pixel values are normalized into  $[0, 1]$ .

**Lemma 1.** In SCI, the function  $f(\mathbf{x}) = \frac{1}{2}\|\mathbf{y} - \mathbf{H}\mathbf{x}\|_2^2$  has bounded gradients, i.e.  $\|\nabla f(\mathbf{x})\|_2 \leq B\|\mathbf{x}\|_2$ .

*Proof.* The full proof is in the Supplementary Material (SM). Here, we show the key steps. The gradient of  $f(\mathbf{x})$  is

$$\nabla f(\mathbf{x}) = \mathbf{H}^\top \mathbf{H}\mathbf{x} - \mathbf{H}^\top \mathbf{y}, \quad (13)$$

where  $\mathbf{H}$  is a block diagonal matrix of size  $n \times nB$  as defined in Eq. (4).  $\mathbf{H}^\top \mathbf{y}$  is non-negative due to the fact that both the measurement  $\mathbf{y}$  and the mask are non-negative in nature, and  $\mathbf{H}^\top \mathbf{H}\mathbf{x}$  is the weighted sum of the  $\mathbf{x}$  and  $\|\mathbf{H}^\top \mathbf{H}\mathbf{x}\|_2 \leq BC_{\max}\|\mathbf{x}\|_2$ , where  $C_{\max}$  is the maximum value in the sensing matrix. Usually, the sensing matrix is normalized to  $[0, 1]$  and this leads to  $C_{\max} = 1$  and therefore  $\|\mathbf{H}^\top \mathbf{H}\mathbf{x}\|_2 \leq B\|\mathbf{x}\|_2$ .

Furthermore, if the mask element  $D_{i,j}$  is drawn from a binary distribution with entries  $\{0, 1\}$  with a probability of  $p_1 \in (0, 1)$  being 1, then  $\|\mathbf{H}^\top \mathbf{H}\mathbf{x}\|_2 \leq p_1 B\|\mathbf{x}\|_2$  with a high probability; usually,  $p_1 = 0.5$  and thus  $\|\mathbf{H}^\top \mathbf{H}\mathbf{x}\|_2 \leq 0.5B\|\mathbf{x}\|_2$ .  $\|\mathbf{H}^\top \mathbf{H}\mathbf{x}\|_2 \leq B\sigma^2\|\mathbf{x}\|_2 \stackrel{\sigma=1}{=} B\|\mathbf{x}\|_2$  In the following, we only consider the non-negative mask being normalized to  $[0, 1]$  in practical systems.  $\square$

Recall that in (4),  $\{\mathbf{D}_i\}_{i=1}^B$  is a diagonal matrix and we denote its diagonal elements by

$$\mathbf{D}_i = \text{diag}(D_{i,1}, \dots, D_{i,n}). \quad (14)$$

Thereby, in SCI,  $\mathbf{H}\mathbf{H}^\top$  is diagonal matrix, i.e.

$$\mathbf{R} = \mathbf{H}\mathbf{H}^\top = \text{diag}(R_1, \dots, R_n), \quad (15)$$

where  $R_j = \sum_{b=1}^B D_{i,j}^2, \forall j = 1, \dots, n$ . We define

$$R_{\max} \stackrel{\text{def}}{=} \max(R_1, \dots, R_n) = \lambda_{\max}(\mathbf{H}\mathbf{H}^\top), \quad (16)$$

$$R_{\min} \stackrel{\text{def}}{=} \min(R_1, \dots, R_n) = \lambda_{\min}(\mathbf{H}\mathbf{H}^\top), \quad (17)$$

where  $\lambda_{\min}(\cdot)$  and  $\lambda_{\max}(\cdot)$  represent the minimum and maximum eigenvalues of the ensured matrix.

**Assumption 1.** We assume that  $\{R_j\}_{j=1}^n > 0$ . This means for each spatial location  $j$ , the  $B$ -frame modulation masks at this location have at least one non-zero entries. We further assume  $R_{\max} > R_{\min}$ .

This assumption makes senses in hardware as we expect at least one out of the  $B$  frames is captured for each pixel during the sensing process. Lemma 1 along with the bounded denoiser in Definition 1 give us the following Corollary.

**Corollary 1.** Consider the sensing model of SCI in (2) and further assume the elements in the sensing matrix satisfying Assumption 3. Given  $\{\mathbf{H}, \mathbf{y}\}$ ,  $\mathbf{x}$  is solved iteratively via PnP-ADMM with bounded denoiser, then  $\mathbf{x}^{(k)}$  and  $\boldsymbol{\theta}^{(k)}$  will converge to a fixed point.

*Proof.* See SM.  $\square$

## 4. Plug-and-Play GAP for SCI

In this section, following the GAP algorithm [21] and the above conditions on PnP-ADMM, we propose PnP-GAP for SCI, which as mentioned before, has a lower computational workload (and thus faster) than PnP-ADMM.

---

### Algorithm 1 Plug-and-Play GAP

---

**Require:**  $\mathbf{H}, \mathbf{y}$ .

- 1: Initial  $\mathbf{v}^{(0)}, \lambda_0, \xi < 1$ .
  - 2: **while** Not Converge **do**
  - 3:   Update  $\mathbf{x}$  by Eq. (65).
  - 4:   Update  $\mathbf{v}$  by denoiser  $\mathbf{v}^{(k+1)} = \mathcal{D}_{\sigma_k}(\mathbf{x}^{(k+1)})$ .
  - 5:   **if**  $\Delta_{k+1} \geq \eta\Delta_k$  **then**
  - 6:      $\lambda_{k+1} = \xi\lambda_k$ ,
  - 7:   **else**
  - 8:      $\lambda_{k+1} = \lambda_k$ .
  - 9:   **end if**
  - 10: **end while**
- 

### 4.1. Algorithm

Different from the ADMM in Eq. (6), GAP solves SCI by the following problem

$$(\hat{\mathbf{x}}, \hat{\mathbf{v}}) = \underset{\mathbf{x}, \mathbf{v}}{\text{argmin}} \frac{1}{2}\|\mathbf{x} - \mathbf{v}\|_2^2 + \lambda g(\mathbf{v}), \text{ s.t. } \mathbf{y} = \mathbf{H}\mathbf{x}. \quad (18)$$

Similarly to ADMM, the minimizer in Eq. (18) is solved by a sequence of (now 2) subproblems and we again let  $k$  denotes the iteration number.

- Solving  $\mathbf{x}$ : given  $\mathbf{v}, \mathbf{x}^{(k+1)}$  is updated via an Euclidean projection of  $\mathbf{v}^{(k)}$  on the linear manifold  $\mathcal{M} : \mathbf{y} = \mathbf{H}\mathbf{x}$ ,

$$\mathbf{x}^{(k+1)} = \mathbf{v}^{(k)} + \mathbf{H}^\top (\mathbf{H}\mathbf{H}^\top)^{-1} (\mathbf{y} - \mathbf{H}\mathbf{v}^{(k)}), \quad (19)$$

where as defined in (15),  $(\mathbf{H}\mathbf{H}^\top)^{-1}$  is fortunately a diagonal matrix and this has been observed and used in a number of SCI inversion problems.

- Solving  $\mathbf{v}$ : given  $\mathbf{x}$ , updating  $\mathbf{v}$  can be seen as an denoising problem and

$$\mathbf{v}^{(k+1)} = \mathcal{D}_\sigma(\mathbf{x}^{(k+1)}). \quad (20)$$

Here, various denoiser can be used with  $\sigma = \sqrt{\lambda}$ .

We can see that in each iteration, the only parameter to be tuned is  $\lambda$  and we thus set  $\lambda_{k+1} = \xi_k \lambda_k$  with  $\xi_k \leq 1$ . Inspired by the PnP-ADMM, we update  $\lambda$  by the following two rules:

- a) Monotone update by setting  $\lambda_{k+1} = \xi \lambda_k$ , with  $\xi < 1$ .
- b) Adaptive update by considering the relative residue:

$$\Delta_{k+1} = \frac{1}{\sqrt{nB}} (\|\mathbf{x}^{(k+1)} - \mathbf{x}^{(k)}\|_2 + \|\mathbf{v}^{(k+1)} - \mathbf{v}^{(k)}\|_2).$$

For any  $\eta \in [0, 1)$  and let  $\xi < 1$  be a constant,  $\lambda_k$  is conditionally updated according to the following settings:



i) If  $\Delta_{k+1} \geq \eta \Delta_k$ , then  $\lambda_{k+1} = \xi \lambda_k$ .

ii) If  $\Delta_{k+1} < \eta \Delta_k$ , then  $\lambda_{k+1} = \lambda_k$ .

With this adaptive updating of  $\lambda_k$ , the full PnP-GAP algorithm for SCI is exhibited in Algorithm 1.

## 4.2. Fixed-point Convergence

In the following, we first prove the fixed point convergence of PnP-GAP and then prove the global convergence in the next subsection. From Eq. (65), we have

$$\begin{aligned} \mathbf{H}\mathbf{x}^{(k+1)} &= \mathbf{H}\mathbf{v}^{(k)} + \mathbf{H}\mathbf{H}^\top(\mathbf{H}\mathbf{H}^\top)^{-1}(\mathbf{y} - \mathbf{H}\mathbf{v}^{(k)}) \\ &= \mathbf{H}\mathbf{v}^{(k)} + \mathbf{y} - \mathbf{H}\mathbf{v}^{(k)} \end{aligned} \quad (21)$$

$$= \mathbf{y}. \quad (22)$$

Similarly,  $\mathbf{y} = \mathbf{H}\mathbf{x}^{(k)}$  and this is the key property of GAP and the main difference between GAP and ADMM.

From (65), we have

$$\mathbf{x}^{(k+1)} - \mathbf{x}^{(k)} = \mathbf{v}^{(k)} - \mathbf{x}^{(k)} + \mathbf{H}^\top(\mathbf{H}\mathbf{H}^\top)^{-1}(\mathbf{y} - \mathbf{H}\mathbf{v}^{(k)}).$$

Following this,

$$\begin{aligned} &\|\mathbf{x}^{(k+1)} - \mathbf{x}^{(k)}\|_2^2 \\ &= \|\mathbf{v}^{(k)} + \mathbf{H}^\top(\mathbf{H}\mathbf{H}^\top)^{-1}(\mathbf{y} - \mathbf{H}\mathbf{v}^{(k)}) - \mathbf{x}^{(k)}\|_2^2 \end{aligned} \quad (23)$$

$$= \|(I - \mathbf{H}^\top(\mathbf{H}\mathbf{H}^\top)^{-1}\mathbf{H})(\mathbf{v}^{(k)} - \mathbf{x}^{(k)})\|_2^2 \quad (24)$$

$$= \|\mathbf{v}^{(k)} - \mathbf{x}^{(k)}\|_2^2 - \|\mathbf{R}^{-\frac{1}{2}}\mathbf{H}(\mathbf{v}^{(k)} - \mathbf{x}^{(k)})\|_2^2 \quad (25)$$

$$\leq \left(1 - \frac{R_{\min}}{R_{\max}}\right) \|\mathbf{v}^{(k)} - \mathbf{x}^{(k)}\|_2^2, \quad (26)$$

where the last two equations following the results of Lemmas 1 and 2 in the SM. This leads to the convergence result below.

**Theorem 1.** *Consider the sensing model of SCI in (2) and further assume the element in the sensing matrix satisfying Assumption 3. Given  $\{\mathbf{H}, \mathbf{y}\}$ ,  $\mathbf{x}$  is solved iteratively via PnP-GAP with bounded denoisers, then  $\mathbf{x}^{(k)}$  and  $\mathbf{v}^{(k)}$  will converge to a fixed point.*

*Proof.* The full proof is in the SM and it follows Eq. (71) and one key result is

$$\|\boldsymbol{\theta}^{(k+1)} - \boldsymbol{\theta}^{(k)}\|_2^2 \leq 7nBC\lambda_0\xi^{k-1}, \quad (27)$$

where  $\boldsymbol{\theta}^{(k)} = (\mathbf{x}^{(k)}, \mathbf{v}^{(k)})$ . The other steps follow the proof of Corollary 1.  $\square$

**Remark 1.** *The above convergence result of PnP-GAP also fits the noisy measurement. In fact, the proof is independent of the noise. This is because the update equation of  $\mathbf{x}^{(k)}$  always satisfying  $\mathbf{y} = \mathbf{H}\mathbf{x}^{(k)}$ . Consider the noisy measurement, i.e.,  $\mathbf{y} = \mathbf{H}\mathbf{x}^* + \mathbf{z}$ , where  $\mathbf{z} \in \mathbb{R}^n$  denotes the measurement noise. Though hereby the measurement  $\mathbf{y}$  is different from the noise free case, we still enforce  $\mathbf{y} = \mathbf{H}\mathbf{x}^{(k)}$  in each iteration.*

It is worth noting that we have proved the fixed point convergence but  $\mathbf{x}^{(k)}$  may not converge to the true signal  $\mathbf{x}^*$ . We show that this global convergence can be proved for PnP-GAP below while it is challenging for PnP-ADMM.

## 4.3. Global Convergence of Plug-and-Play GAP

We first make the following assumption.

**Assumption 2.** *There is only a single true signal  $\mathbf{x}^*$  satisfying the measurement model  $\mathbf{y} = \mathbf{H}\mathbf{x}^*$  in SCI.*

We understand that in real cases, there might be more than one signal satisfying  $\mathbf{y} = \mathbf{H}\mathbf{x}$  and this forward model might be an (linear) approximation of the physical imaging system. By using this assumption, we have the following global convergence result of PnP-GAP.

**Theorem 2.** *[Global convergence of PnP-GAP] Consider the sensing model of SCI in (2) and further assume the element in the sensing matrix satisfying Assumption 3. Consider the true signal  $\mathbf{y} = \mathbf{H}\mathbf{x}^*$ . Given  $\{\mathbf{H}, \mathbf{y}\}$ ,  $\hat{\mathbf{x}}$  is solved iteratively via PnP-GAP with bounded denoisers. For a constant  $C_g > 0$  and  $0 < \varphi < 1$*

$$\|\mathbf{x}^{(k+1)} - \mathbf{x}^*\|_2 \leq \sqrt{1 - \frac{R_{\min}}{R_{\max}}} \|\mathbf{x}^{(k)} - \mathbf{x}^*\|_2 + C_g\varphi^k. \quad (28)$$

*Proof.* Let us start from (65); we have

$$\begin{aligned} \mathbf{x}^{(k+1)} - \mathbf{x}^* &= \mathbf{v}^{(k)} - \mathbf{x}^* + \mathbf{H}^\top(\mathbf{H}\mathbf{H}^\top)^{-1}(\mathbf{y} - \mathbf{H}\mathbf{v}^{(k)}) \\ &= \mathbf{v}^{(k)} - \mathbf{x}^* + \mathbf{H}^\top(\mathbf{H}\mathbf{H}^\top)^{-1}\mathbf{H}(\mathbf{x}^* - \mathbf{v}^{(k)}). \end{aligned} \quad (29)$$

Following the derivation in (70), we have

$$\begin{aligned} \|\mathbf{x}^{(k+1)} - \mathbf{x}^*\|_2^2 &= \|\mathbf{v}^{(k)} - \mathbf{x}^*\|_2^2 - \|\mathbf{R}^{-\frac{1}{2}}\mathbf{H}(\mathbf{v}^{(k)} - \mathbf{x}^*)\|_2^2 \\ &\leq \left(1 - \frac{R_{\min}}{R_{\max}}\right) \|\mathbf{v}^{(k)} - \mathbf{x}^*\|_2^2. \end{aligned} \quad (30)$$

This is

$$\|\mathbf{x}^{(k+1)} - \mathbf{x}^*\|_2 \leq \sqrt{1 - \frac{R_{\min}}{R_{\max}}} \|\mathbf{v}^{(k)} - \mathbf{x}^*\|_2 \quad (31)$$

$$\leq \sqrt{1 - \frac{R_{\min}}{R_{\max}}} (\|\mathbf{v}^{(k)} - \mathbf{x}^{(k)}\|_2 + \|\mathbf{x}^{(k)} - \mathbf{x}^*\|_2) \quad (32)$$

$$\leq \sqrt{1 - \frac{R_{\min}}{R_{\max}}} \|\mathbf{x}^{(k)} - \mathbf{x}^*\|_2 + \sqrt{nBC\sigma_{k-1}(1 - \frac{R_{\min}}{R_{\max}})} \quad (33)$$

$$= \sqrt{1 - \frac{R_{\min}}{R_{\max}}} \|\mathbf{x}^{(k)} - \mathbf{x}^*\|_2 + \lambda_0 \sqrt{nBC(1 - \frac{R_{\min}}{R_{\max}})} \xi^{\frac{k-1}{4}}, \quad (34)$$

where Eqs. (33)-(34) are from the proof of Theorem 1 in the SM. Note that since  $\sqrt{1 - \frac{R_{\min}}{R_{\max}}} < 1$  and  $\xi < 1$  and therefore, when  $k \rightarrow \infty$ ,

$$\lambda_0 \sqrt{nBC(1 - \frac{R_{\min}}{R_{\max}})} \xi^{\frac{k-1}{4}} \rightarrow 0. \quad (35)$$

In (28), we have defined

$$C_g = \lambda_0 \sqrt{nBC(1 - \frac{R_{\min}}{R_{\max}})} \xi^{-\frac{1}{4}}, \quad \varphi = \xi^{\frac{1}{4}}. \quad (36)$$

The desired global convergence results follows.  $\square$

Note that we have assumed  $R_{\min} < R_{\max}$  in Assumption 3. Otherwise, Theorem 2 leads to  $\|\mathbf{x}^{(k+1)} - \mathbf{x}^*\|_2 = 0$ .

**Theorem 3.** [Stable convergence of PnP-GAP] Consider the same conditions in Theorem 2 but now the noisy measurement  $\mathbf{y} = \mathbf{H}\mathbf{x}^* + \mathbf{z}$  and  $\|\mathbf{z}\|_2 \leq \epsilon$ . Given  $\{\mathbf{H}, \mathbf{y}\}$ ,  $\hat{\mathbf{x}}$  is solved iteratively via PnP-GAP with bounded denoisers. For a constant  $C_g > 0$  and  $0 < \varphi < 1$

$$\|\mathbf{x}^{(k+1)} - \mathbf{x}^*\|_2 \leq \sqrt{1 - \frac{R_{\min}}{R_{\max}}} \|\mathbf{x}^{(k)} - \mathbf{x}^*\|_2 + C_g \varphi^k + \frac{\epsilon}{\sqrt{R_{\min}}}.$$

*Proof.* Different from (29), where  $\mathbf{y} = \mathbf{H}\mathbf{x}^*$  was used, now we have (full details in the SM)

$$\begin{aligned} \mathbf{x}^{(k+1)} - \mathbf{x}^* &= [\mathbf{I} - \mathbf{H}^\top (\mathbf{H}\mathbf{H}^\top)^{-1} \mathbf{H}] (\mathbf{x}^* - \mathbf{v}^{(k)}) \\ &\quad + \mathbf{H}^\top (\mathbf{H}\mathbf{H}^\top)^{-1} \mathbf{z}. \end{aligned} \quad (37)$$

Taking  $\ell_2$ -norm on both sides and using the results of (97) with some derivations,

$$\|\mathbf{x}^{(k+1)} - \mathbf{x}^*\|_2^2 \leq (1 - \frac{R_{\min}}{R_{\max}}) \|\mathbf{v}^{(k)} - \mathbf{x}^*\|_2^2 + \frac{1}{R_{\min}} \|\mathbf{z}\|_2^2.$$

Using the result of (34) and  $\sqrt{a+b} \leq \sqrt{a} + \sqrt{b}$ ,

$$\begin{aligned} \|\mathbf{x}^{(k+1)} - \mathbf{x}^*\|_2 &\leq \sqrt{1 - \frac{R_{\min}}{R_{\max}}} \|\mathbf{x}^{(k)} - \mathbf{x}^*\|_2 \\ &\quad + \lambda_0 \sqrt{nBC(1 - \frac{R_{\min}}{R_{\max}})} \xi^{\frac{k-1}{4}} + \frac{\epsilon}{\sqrt{R_{\min}}}. \end{aligned} \quad (38)$$

The final result follows.  $\square$

It is worth noting that by assuming WNNM being a bounded denoiser, DeSCI [22], which is GAP-WNNM, is a special case of our PnP-GAP.

#### 4.4. PnP-ADMM vs. PnP-GAP

Comparing PnP-GAP in Eqs (65)-(20) and PnP-ADMM in Eqs (7)-(9), we can see that PnP-GAP only has two sub-problems (rather than three as in PnP-ADMM) and thus the computation is faster. It was pointed out in [22] that in the noise-free case, ADMM and GAP perform the same and this has been mathematically proved. However, in the noisy case, ADMM usually performs better since it considered noise in the model and below we give a geometrical explanation.

As shown in Fig. 3, where we used a two-dimensional sparse signal as an example, we can see that since GAP imposes  $\mathbf{y} = \mathbf{H}\hat{\mathbf{x}}$ , the solution of GAP  $\hat{\mathbf{x}}$  is always on the dash-green line (due to noise, this line might be deviated from the solid green line where the true signal lies on). However, the solution of ADMM does not have this constraint but to minimize  $\|\mathbf{y} - \mathbf{H}\mathbf{x}\|_2^2$ , which can be in the dash-red circle or the yellow-dash circle depending on the initialization. In the noise-free case, both GAP and ADMM will have a large chance to converge to the true signal  $\mathbf{x}^*$ . However, in the noisy case, the Euclidean distance between GAP solution and the true signal ( $\|\hat{\mathbf{x}} - \mathbf{x}^*\|_2$ ) might be larger than that of ADMM. Again, the final solution of ADMM depends on the initialization and it is not guaranteed to be more accurate than that of GAP.

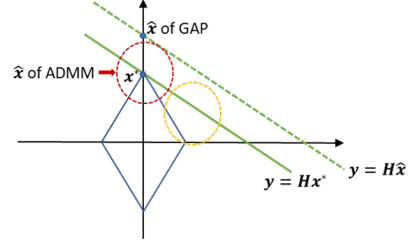


Figure 3. Demonstration of the solution of ADMM (within the dash-red circle or dash-yellow circle depending on the initialization) and GAP ( $\hat{\mathbf{x}}$ ) under the noisy case. The difference is that the solution of GAP always lies on  $\mathbf{y} = \mathbf{H}\hat{\mathbf{x}}$ .

### 5. Integrate Various Denoisers into PnP for SCI Reconstruction

It can be seen from Eq. (28) in Theorem 2 that the reconstruction error term depends on  $C_g \varphi^k$ , and from (103), we observe that while  $\{n, B, R_{\min}, R_{\max}\}$  are fixed, and  $\{\lambda_0, \xi\}$  are pre-set or tuned, only  $C$  depends on the bounded denoising algorithm. In other words, a better denoiser with a smaller  $C$  can provide a reconstruction result closer to the true signal. Various denoising algorithms exist for different tasks based on speed and quality. Usually, a faster denoiser *e.g.*, TV, is very efficient, but cannot provide high-quality results. The middle class algorithms *e.g.*, BM3D [10] can provide decent results with a longer running time. More advanced denoising algorithm, *e.g.*, WNNM [14, 13] can provide better results [22], but even slower. Another line of emerging denoising approaches is based on deep learning [48, 74], which can provide decent results within a short time after training, but they are usually not robust to noise levels and in high noisy cases, the results are not good. Different from conventional denoising problems, in SCI reconstruction, the noise level in each iteration is usually from large to small and the dynamic range can from 150 to 1, considering the pixel values within  $\{0, 1, \dots, 255\}$ . Fortunately, FFDNet [75] has provided us a fast and flexible solution under various noise levels.

By integrating these denoising algorithms into PnP-GAP/ADMM, we can have different algorithms (Table 1 and Fig. 2) with different results. It is worth noting that DeSCI can be seen as PnP-WNNM, and its best results are achieved by exploiting the correlation across different video frames. On the other hand, most existing deep denoising priors are still based on images. Therefore, it is expected that the results of PnP-GAP/ADMM-FFDNet are not as good as DeSCI. We anticipate that with the advances of deep denoising priors, better video denoising method will boost the our PnP-based SCI reconstruction results. In addition, these different denoisers can be used in parallel, *i.e.*, one after each other in one GAP/ADMM iteration or used sequentially, *i.e.*, the first  $K_1$  iterations using FFDNet and the next  $K_2$  iterations using WNNM to achieve better results.

Table 1. The average results of PSNR in dB (left entry in each cell) and SSIM (right entry in each cell) and run time per measurement/shot in minutes by different algorithms on 6 benchmark datasets.

Algorithm	Kobe	Traffic	Runner	Drop	Crash	Aerial	Average	Run time (min)
GAP-TV	26.46, 0.8848	20.89, 0.7148	28.52, 0.9092	34.63, 0.9704	24.82, 0.8383	25.05, 0.8281	26.73, 0.8576	0.07
DeSCI (GAP-WNNM)	<b>33.25</b> , 0.9518	<b>28.71</b> , <b>0.9250</b>	<b>38.48</b> , <b>0.9693</b>	43.10, 0.9925	<b>27.04</b> , <b>0.9094</b>	25.33, 0.8603	<b>32.65</b> , <b>0.9347</b>	103.0
PnP-VBM4D	30.60, 0.9260	26.60, 0.8958	30.10, 0.9271	26.58, 0.8777	25.30, 0.8502	26.89, 0.8521	27.68, 0.8882	7.9
PnP-FFDNet	30.50, 0.9256	24.18, 0.8279	32.15, 0.9332	40.70, 0.9892	25.42, 0.8493	25.27, 0.8291	29.70, 0.8924	<b>0.05</b> (GPU)
PnP-WNNM-TV	33.00, 0.9520	26.76, 0.9035	38.00, 0.9690	43.27, 0.9927	26.25, 0.8972	25.53, 0.8595	32.14, 0.9290	40.8
PnP-WNNM-VBM4D	33.08, <b>0.9537</b>	28.05, 0.9191	33.73, 0.9632	28.82, 0.9289	26.56, 0.8874	<b>27.74</b> , <b>0.8852</b>	29.66, 0.9229	25.0
PnP-WNNM-FFDNet	32.54, 0.9511	26.00, 0.8861	36.31, 0.9664	<b>43.45</b> , <b>0.9930</b>	26.21, 0.8930	25.83, 0.8618	31.72, 0.9252	17.9

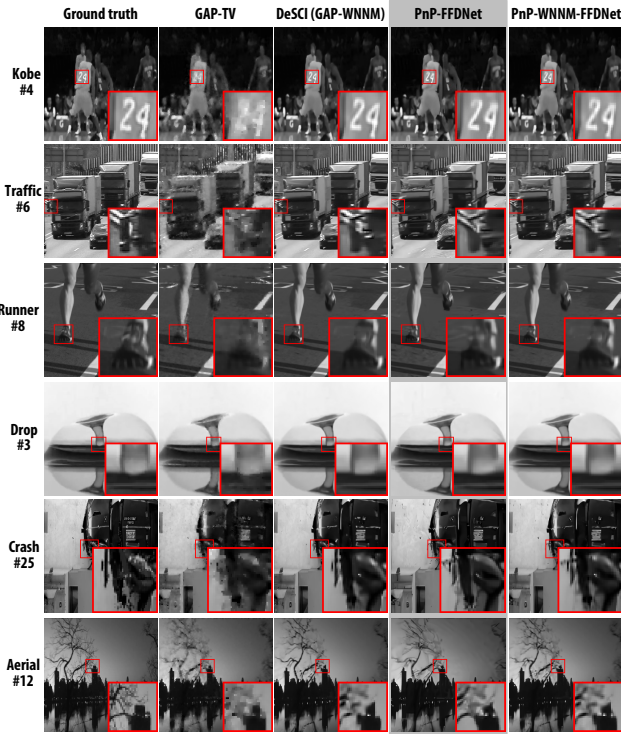


Figure 4. Reconstructed frames of PnP-GAP algorithms (GAP-TV, PnP-FFDNet, DeSCI (GAP-WNNM), PnP-WNNM-FFDNet) on six simulated benchmark video SCI datasets.

## 6. Results

We applied the proposed PnP algorithms to both simulation [22, 26] and real datasets captured by the SCI cameras [23, 61]. Conventional denoising algorithms include TV [53], VBM4D [27] and WNNM [14] are used. For the deep learning based denoiser, we have tried various algorithms and found that FFDNet [75] provides the best results.

**Simulation: Benchmark Data** We follow the simulation setup in [22] using the six datasets, *i.e.*, Kobe, Traffic, Runner, Drop, crash, and aerial [26], where  $B = 8$  video frames are compressed into a single measurement. Table 1 summarizes the PSNR and SSIM [47] results of these 6 benchmark data using various denoising algorithms, where DeSCI can be categorized as GAP-WNNM, and PnP-WNNM-FFDNet used 50 iterations FFDNet and then 60 iterations WNNM, similar for GAP-WNNM-VBM4D. It can be observed that: *i)* By using GPU, PnP-

FFDNet is now the fastest algorithm<sup>1</sup>; it is even faster than GAP-TV, meanwhile providing about 3dB higher PSNR than GAP-TV. Therefore, PnP-FFDNet can be used as an *efficient baseline* in SCI reconstruction. Since the average PSNR is close to 30dB, it is applicable in real cases. This will be further verified in the following subsection on large-scale datasets. *ii)* DeSCI still provides the best results on average; however, by combining other algorithms with WNNM, comparable results (*e.g.* PnP-WNNM-FFDNet) can be achieved by only using 1/6 computational time. Fig. 4 plots selected frames of the six datasets using different algorithms. It can be seen that though GAP-WNNM still leads to best results, the difference between PnP-FFDNet and DeSCI is very small and in most cases, they are close to each other.

**Simulation: Large-scale Data** We hereby show the results of large-scale data results in Fig. 5, where all videos (in SM) are reconstructed from a snapshot with sizes from  $1920 \times 1080 \times 24$  to  $3840 \times 1644 \times 48$ . It is worth noting that only GAP-TV and PnP-FFDNet can be used as all other algorithms are too slow (more than 10 hours) to run<sup>2</sup>. In general, PnP-FFDNet provides more than 4dB higher PSNR than GAP-TV. Please pay attention to the details recovered by PnP-FFDNet. These results along with the high speed can lead to real applications of SCI in our daily life videos.

**Real Data** Lastly, we apply the proposed PnP framework to real data captured by SCI cameras to verify the robustness of the algorithms. Figs. 6-7 show the results of different compression ratios and different sizes. It can be observed that in most cases, PnP-FFDNet can provide comparable or even better (*chopper wheel*) results than DeSCI but again with a significant saving on computational time. The running time of these data using different algorithms is shown in Table 2, where we can see that PnP-FFDNet provides results around 12 seconds even for a  $512 \times 512 \times 22$  large-scale video.

<sup>1</sup>Only a regular GPU is needed to run FFDNet and since FFDNet is performed in a frame-wise manner, we do not need a large amount of CPU or GPU RAM (no more than 2GB here) compared to other video denoisers using parallization (even with parallelization, other algorithms listed here are unlikely to outperform PnP-FFDNet in terms of speed).

<sup>2</sup>These large-scale datasets are of different sizes and different compression rates. From the speed perspective, it might be able to train (big and deep) networks for each of them. But this will need a significant amount of computational resources (GPUs with large memory) and training data and time. By contrast, our PnP-FFDNet provides a good trade-off of speed, accuracy and flexibility, since we don't need to re-train the model.





Figure 5. Reconstructed frames of PnP-GAP algorithms (GAP-TV and PnP-FFDNet) on four simulated large-scale video SCI datasets.

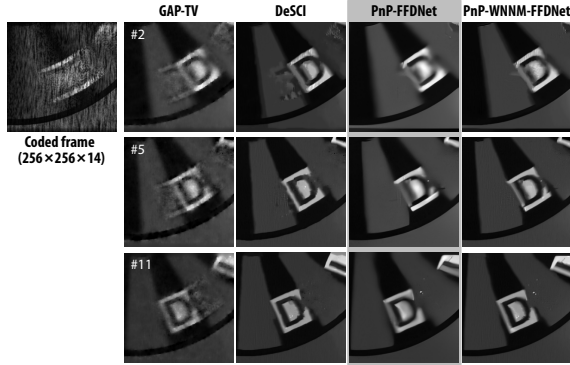


Figure 6. Real data: chopper wheel ( $256 \times 256 \times 14$ ).

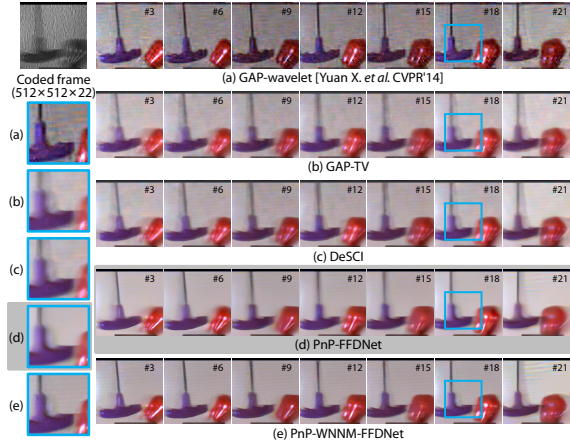


Figure 7. Real data: hammer color video SCI ( $512 \times 512 \times 22$ ).

Table 2. Running time (second) of real data using different algorithms. Visual results of labs and UCF are shown in the SM.

Real dataset	Pixel resolution	GAP-TV	DeSCI	PnP-FFDNet	PnP-WNNM-FFDNet
chopperwheel	$256 \times 256 \times 14$	11.6	3185.8	2.7	1754.7
labs	$484 \times 248 \times 10$	36.9	6471.3	4.5	3226.5
hammer color	$512 \times 512 \times 22$	94.5	4791.0	12.6	1619.4
UCF	$1100 \times 850 \times 10$	300.8	2938.8*	12.5	1504.5*

\* WNNM is performed in a frame-wise manner for large-scale datasets.

## 7. Conclusions

We proposed plug-and-play algorithms for the reconstruction of snapshot compressive video imaging systems. By integrating deep denoisers into the PnP framework, we not only get excellent results on both simulation and real datasets, but also provide reconstruction in a short time with sufficient flexibility. Convergence results of PnP-GAP are proved and we first time show that SCI can be used in large-scale (HD, FHD and UHD) daily life videos. This paves the way of practical applications of SCI.

Regarding the future work, one direction is to train a better video (rather than image) denoising network and apply it to the proposed PnP framework to further improve the reconstruction results. The other direction is to build a real large-scale video SCI system to be used in advanced cameras [4].

**Acknowledgments.** The work of Jinli Suo and Qionghai Dai is partially supported by NSFC 61722110, 61931012, 61631009 and Beijing Municipal Science & Technology Commission (BMSTC) (No. Z181100003118014).

## A. Proof of Lemma 1: Bounded Gradients of $f(\mathbf{x})$

*Proof.* The gradient of  $f(\mathbf{x})$  in SCI is

$$\nabla f(\mathbf{x}) = \mathbf{H}^\top \mathbf{H} \mathbf{x} - \mathbf{H}^\top \mathbf{y}, \quad (39)$$

where  $\mathbf{H}$  is a block diagonal matrix of size  $n \times nB$ .

- The  $\mathbf{H}^\top \mathbf{y}$  is a non-negative constant since both the measurement  $\mathbf{y}$  and the mask are non-negative in nature.
- Now let's focus on  $\mathbf{H}^\top \mathbf{H} \mathbf{x}$ . Since

$$\begin{aligned} \mathbf{H}^\top \mathbf{H} &= \begin{bmatrix} D_1 \\ \vdots \\ D_B \end{bmatrix} [D_1 \dots D_B] \\ &= \begin{bmatrix} D_1^2 & D_1 D_2 & \dots & D_1 D_B \\ D_1 D_2 & D_2^2 & \dots & D_2 D_B \\ \vdots & \vdots & \ddots & \vdots \\ D_1 D_B & D_2 D_B & \dots & D_B^2 \end{bmatrix}, \end{aligned} \quad (40)$$

due to this special structure,  $\mathbf{H}^\top \mathbf{H} \mathbf{x}$  is the weighted sum of the  $\mathbf{x}$  and  $\|\mathbf{H}^\top \mathbf{H} \mathbf{x}\|_2 \leq BC_{\max} \|\mathbf{x}\|_2$ , where  $C_{\max}$  is the maximum value in the sensing matrix. Usually, the sensing matrix is normalized to  $[0, 1]$  and this leads to  $C_{\max} = 1$  and therefore  $\|\mathbf{H}^\top \mathbf{H} \mathbf{x}\|_2 \leq B \|\mathbf{x}\|_2$ .

Thus,  $\nabla f(\mathbf{x})$  is bounded. Furthermore,

- If the mask element  $D_{i,j}$  is drawn from a binary distribution with entries  $\{0, 1\}$  with a property of  $p_1 \in (0, 1)$  being 1, then

$$\|\mathbf{H}^\top \mathbf{H} \mathbf{x}\|_2 \leq p_1 B \|\mathbf{x}\|_2 \quad (42)$$

with a high probability; usually,  $p_1 = 0.5$  and thus  $\|\mathbf{H}^\top \mathbf{H} \mathbf{x}\|_2 \leq 0.5B \|\mathbf{x}\|_2$ .

- If the mask element  $D_{i,j}$  is drawn from a Gaussian distribution  $\mathcal{N}(0, \sigma^2)$  as in [17, 18], though it is not practical to get negative modulation (values of  $D_{i,j}$  in hardware,

$$\|\mathbf{H}^\top \mathbf{H} \mathbf{x}\|_2 \leq B\sigma^2 \|\mathbf{x}\|_2 \stackrel{\sigma=1}{=} B \|\mathbf{x}\|_2, \quad (43)$$

with a high probability.

□

## B. Proof of Theorem 1: Fixed-point Convergence of Plug-and-Play GAP

Before we show the full proof, we first present 2 lemmas, which are important and based on the special structure of SCI sensing matrix.

Recall Assumption 1 in the main paper.

**Assumption 3.** We assume that  $\{R_j\}_{j=1}^n > 0$ . This means for each spatial location  $j$ , the  $B$  frame modulation masks at this location have at least one non-zero entries. We further assume  $R_{\max} > R_{\min}$ .

**Lemma 2.** For any  $\mathbf{x} \in \mathbb{R}^{nB}$ , consider  $D_{i,j}, i = 1, \dots, B; j = 1, \dots, n$  satisfy Assumption 3, then

$$\begin{aligned} \frac{R_{\min}}{R_{\max}} \|\mathbf{x}\|_2^2 &\leq \|\mathbf{H}^\top (\mathbf{H} \mathbf{H}^\top)^{-1} \mathbf{H} \mathbf{x}\|_2^2 \\ &= \|\mathbf{R}^{-\frac{1}{2}} \mathbf{H} \mathbf{x}\|_2^2 \leq \|\mathbf{x}\|_2^2. \end{aligned} \quad (44)$$

*Proof.*

$$\begin{aligned} &\|\mathbf{H}^\top (\mathbf{H} \mathbf{H}^\top)^{-1} \mathbf{H} \mathbf{x}\|_2^2 \\ &= \mathbf{x}^\top \mathbf{H}^\top (\mathbf{H} \mathbf{H}^\top)^{-1} \mathbf{H} \mathbf{H}^\top (\mathbf{H} \mathbf{H}^\top)^{-1} \mathbf{H} \mathbf{x} \end{aligned} \quad (45)$$

$$= \mathbf{x}^\top \mathbf{H}^\top \mathbf{R}^{-1} \mathbf{H} \mathbf{x} \quad (46)$$

$$= \|\mathbf{R}^{-\frac{1}{2}} \mathbf{H} \mathbf{x}\|_2^2. \quad (47)$$

Further

$$\|\mathbf{R}^{-\frac{1}{2}} \mathbf{H} \mathbf{x}\|_2^2 = \sum_{j=1}^n \left[ \frac{\sum_{i=1}^B D_{i,j} x_{i,j}}{\sqrt{R_j}} \right]^2 \quad (48)$$

$$= \sum_{j=1}^n \frac{(D_{1,j} x_{1,j} + \dots + D_{B,j} x_{B,j})^2}{R_j} \quad (49)$$

Recall that  $R_j = \sum_{i=1}^B D_{i,j}^2 > 0$ , and  $D_{i,j} \geq 0, \forall i = 1, \dots, B$  by Assumption 3. Furthermore,  $\forall j$ , at least one element in  $\left\{ \frac{D_{1,j}}{\sqrt{R_j}}, \dots, \frac{D_{B,j}}{\sqrt{R_j}} \right\}$  is larger than 0 and we denotes it by  $\frac{D_{i^*,j}}{\sqrt{R_j}} > 0$ . Following this,

$$\|\mathbf{R}^{-\frac{1}{2}} \mathbf{H} \mathbf{x}\|_2^2 = \sum_{j=1}^n \frac{(D_{i^*,j} x_{i^*,j} + \dots + D_{B,j} x_{B,j})^2}{D_{1,j}^2 + \dots + D_{B,j}^2} \quad (50)$$

$$= \sum_{j=1}^n \frac{(\sum_{i=1}^B D_{i,j} x_{i,j})^2}{\sum_{i=1}^B D_{i,j}^2} \leq \sum_{j=1}^n \sum_{i=1}^B \frac{D_{i,j}^2 x_{i,j}^2}{D_{i,j}^2} \quad (51)$$

$$= \sum_{j=1}^n \sum_{i=1}^B x_{i,j}^2 = \|\mathbf{x}\|_2^2, \quad (52)$$

where (51) is from the Cauchy-Schwarz inequality by defining the following two vectors

$$\mathbf{d}_j = [D_{1,j}, \dots, D_{B,j}]^\top, \quad (53)$$

$$\mathbf{x}_j = [x_{1,j}, \dots, x_{B,j}]^\top, \quad (54)$$

and  $\langle \mathbf{d}_j, \mathbf{x}_j \rangle^2 \leq \|\mathbf{d}_j\|_2^2 \|\mathbf{x}_j\|_2^2$ .

Since we have assumed  $D_{i,j} \geq 0$  and at least one element in  $\mathbf{d}_j$  is larger than 0, the equality  $\|\mathbf{R}^{-\frac{1}{2}} \mathbf{H} \mathbf{x}\|_2^2 = \|\mathbf{x}\|_2^2$  only



happens when  $\mathbf{x} = \mathbf{0}$  or  $\mathbf{x}_j = c\mathbf{d}_j$ , where  $c$  is a constant and this means  $\mathbf{x}_j$  and  $\mathbf{d}_j$  are linearly dependent.

This will be an extreme case and this means the signal is linearly dependent on the mask and thus the SCI system cannot resolve the signal.

Recall that  $\mathbf{R} = \mathbf{H}\mathbf{H}^\top$  is a diagonal matrix and  $\lambda_{\min}(\mathbf{H}\mathbf{H}^\top) = R_{\min}$ ,  $\lambda_{\max}(\mathbf{H}\mathbf{H}^\top) = R_{\max}$ . We have

$$R_{\min}\|\mathbf{x}\|_2^2 \leq \|\mathbf{H}\mathbf{x}\|_2^2 \leq R_{\max}\|\mathbf{x}\|_2^2 \quad (55)$$

Following this and  $\mathbf{R}^{-1} = \text{diag}(R_1^{-1}, \dots, R_n^{-1})$ , we have

$$\frac{R_{\min}}{R_{\max}}\|\mathbf{x}\|_2^2 \leq \|\mathbf{R}^{-\frac{1}{2}}\mathbf{H}\mathbf{x}\|_2^2 \leq \frac{R_{\max}}{R_{\min}}\|\mathbf{x}\|_2^2. \quad (56)$$

Along with (52), we have

$$\frac{R_{\min}}{R_{\max}}\|\mathbf{x}\|_2^2 \leq \|\mathbf{R}^{-\frac{1}{2}}\mathbf{H}\mathbf{x}\|_2^2 \leq \|\mathbf{x}\|_2^2, \quad (57)$$

which is the desired result.  $\square$

**Lemma 3.** For any  $\mathbf{x} \in \mathbb{R}^{nB}$ , consider  $D_{i,j}, i = 1, \dots, B; j = 1, \dots, n$  satisfy Assumption 3, then

$$\|(\mathbf{I} - \mathbf{H}^\top(\mathbf{H}\mathbf{H}^\top)^{-1}\mathbf{H})\mathbf{x}\|_2^2 = \|\mathbf{x}\|_2^2 - \|\mathbf{R}^{-\frac{1}{2}}\mathbf{H}\mathbf{x}\|_2^2. \quad (58)$$

*Proof.*

$$\begin{aligned} & \|(\mathbf{I} - \mathbf{H}^\top(\mathbf{H}\mathbf{H}^\top)^{-1}\mathbf{H})\mathbf{x}\|_2^2 \\ &= \|\mathbf{x} - \mathbf{H}^\top(\mathbf{H}\mathbf{H}^\top)^{-1}\mathbf{H}\mathbf{x}\|_2^2 \\ &= [\mathbf{x} - \mathbf{H}^\top(\mathbf{H}\mathbf{H}^\top)^{-1}\mathbf{H}\mathbf{x}]^\top [\mathbf{x} - \mathbf{H}^\top(\mathbf{H}\mathbf{H}^\top)^{-1}\mathbf{H}\mathbf{x}] \end{aligned} \quad (59)$$

$$\begin{aligned} &= \mathbf{x}^\top \mathbf{x} - 2\mathbf{x}^\top \mathbf{H}^\top(\mathbf{H}\mathbf{H}^\top)^{-1}\mathbf{H}\mathbf{x} \\ &\quad + \mathbf{x}^\top \mathbf{H}^\top(\mathbf{H}\mathbf{H}^\top)^{-1}\mathbf{H}\mathbf{H}^\top(\mathbf{H}\mathbf{H}^\top)^{-1}\mathbf{H}\mathbf{x} \end{aligned} \quad (61)$$

$$= \mathbf{x}^\top \mathbf{x} - \mathbf{x}^\top \mathbf{H}^\top(\mathbf{H}\mathbf{H}^\top)^{-1}\mathbf{H}\mathbf{x} \quad (62)$$

$$= \|\mathbf{x}\|_2^2 - \|\mathbf{R}^{-\frac{1}{2}}\mathbf{H}\mathbf{x}\|_2^2, \quad (63)$$

where we have used  $\mathbf{R} = \mathbf{H}\mathbf{H}^\top$ .

Along with Lemma 2, we have

$$\|(\mathbf{I} - \mathbf{H}^\top(\mathbf{H}\mathbf{H}^\top)^{-1}\mathbf{H})\mathbf{x}\|_2^2 \leq \left(1 - \frac{R_{\min}}{R_{\max}}\right)\|\mathbf{x}\|_2^2. \quad (64)$$

$\square$

Now we prove Theorem 1 in the main paper.

*Proof.* From (21) in the main paper,

$$\mathbf{x}^{(k+1)} = \mathbf{v}^{(k)} + \mathbf{H}^\top(\mathbf{H}\mathbf{H}^\top)^{-1}(\mathbf{y} - \mathbf{H}\mathbf{v}^{(k)}), \quad (65)$$

we have

$$\mathbf{x}^{(k+1)} - \mathbf{x}^{(k)} = \mathbf{v}^{(k)} - \mathbf{x}^{(k)} + \mathbf{H}^\top(\mathbf{H}\mathbf{H}^\top)^{-1}(\mathbf{y} - \mathbf{H}\mathbf{v}^{(k)}), \quad (66)$$

Following this,

$$\|\mathbf{x}^{(k+1)} - \mathbf{x}^{(k)}\|_2^2 \quad (67)$$

$$= \|\mathbf{v}^{(k)} + \mathbf{H}^\top(\mathbf{H}\mathbf{H}^\top)^{-1}(\mathbf{y} - \mathbf{H}\mathbf{v}^{(k)}) - \mathbf{x}^{(k)}\|_2^2 \quad (68)$$

$$= \|\mathbf{v}^{(k)} + \mathbf{H}^\top(\mathbf{H}\mathbf{H}^\top)^{-1}(\mathbf{H}\mathbf{x}^{(k)} - \mathbf{H}\mathbf{v}^{(k)}) - \mathbf{x}^{(k)}\|_2^2$$

$$= \|(\mathbf{I} - \mathbf{H}^\top(\mathbf{H}\mathbf{H}^\top)^{-1}\mathbf{H})(\mathbf{v}^{(k)} - \mathbf{x}^{(k)})\|_2^2 \quad (69)$$

$$= \|\mathbf{v}^{(k)} - \mathbf{x}^{(k)}\|_2^2 - \|\mathbf{R}^{-\frac{1}{2}}\mathbf{H}(\mathbf{v}^{(k)} - \mathbf{x}^{(k)})\|_2^2 \quad (70)$$

$$\leq \left(1 - \frac{R_{\min}}{R_{\max}}\right)\|\mathbf{v}^{(k)} - \mathbf{x}^{(k)}\|_2^2, \quad (71)$$

where the last equation (71) comes from Lemma 3. Now let's use  $\mathbf{v}^{(k)} = \mathcal{D}_{\sigma_{k-1}}(\mathbf{x}^{(k)})$  and the definition of bounded denoiser

$$\|\mathbf{x}^{(k+1)} - \mathbf{x}^{(k)}\|_2^2 \leq \left(1 - \frac{R_{\min}}{R_{\max}}\right)\|\mathbf{v}^{(k)} - \mathbf{x}^{(k)}\|_2^2 \quad (72)$$

$$= \left(1 - \frac{R_{\min}}{R_{\max}}\right)\|\mathcal{D}_{\sigma_{k-1}}(\mathbf{x}^{(k)}) - \mathbf{x}^{(k)}\|_2^2 \quad (73)$$

$$\leq nBC \left(1 - \frac{R_{\min}}{R_{\max}}\right)\sigma_{k-1}^2 \quad (74)$$

$$= nBC \left(1 - \frac{R_{\min}}{R_{\max}}\right)\lambda_{k-1}, \quad (75)$$

where we have used  $\sigma_{k-1} = \sqrt{\lambda_{k-1}}$ .

Based on this,

$$\begin{aligned} & \|\mathbf{v}^{(k+1)} - \mathbf{v}^{(k)}\|_2^2 \\ &= \|\mathcal{D}_{\sigma_k}(\mathbf{x}^{(k+1)}) - \mathcal{D}_{\sigma_{k-1}}(\mathbf{x}^{(k)})\|_2^2 \end{aligned} \quad (76)$$

$$\begin{aligned} &= \|\mathcal{D}_{\sigma_k}(\mathbf{x}^{(k+1)}) - \mathbf{x}^{(k+1)} \\ &\quad + \mathbf{x}^{(k+1)} - \mathbf{x}^{(k)} + \mathbf{x}^{(k)} - \mathcal{D}_{\sigma_{k-1}}(\mathbf{x}^{(k)})\|_2^2 \end{aligned} \quad (77)$$

$$\begin{aligned} &\leq 2\|\mathcal{D}_{\sigma_k}(\mathbf{x}^{(k+1)}) - \mathbf{x}^{(k+1)}\|_2^2 \\ &\quad + 2\|\mathbf{x}^{(k+1)} - \mathbf{x}^{(k)}\|_2^2 + 2\|\mathbf{x}^{(k)} - \mathcal{D}_{\sigma_{k-1}}(\mathbf{x}^{(k)})\|_2^2 \\ &\leq 2nBC\lambda_k + 2nBC \left(1 - \frac{R_{\min}}{R_{\max}}\right)\lambda_{k-1} + 2nBC\lambda_{k-1} \end{aligned} \quad (78)$$

$$\begin{aligned} &\stackrel{\lambda_k \leq \lambda_{k-1}}{\leq} \left(6nBC - \frac{2nBCR_{\min}}{R_{\max}}\right)\lambda_{k-1}, \end{aligned} \quad (79)$$

Following [9], we define  $\boldsymbol{\theta}^{(k)} = (\mathbf{x}^{(k)}, \mathbf{v}^{(k)})$ . Let  $\Theta$  be the domain of  $\boldsymbol{\theta}^{(k)}$  for all  $k$ . On  $\Theta$ , we define a distance function  $D : \Theta \times \Theta \rightarrow \mathbb{R}$  such that

$$D(\boldsymbol{\theta}^{(k)}, \boldsymbol{\theta}^{(j)}) = \frac{1}{nB} \left( \|\mathbf{x}^{(k)} - \mathbf{x}^{(j)}\|_2^2 + \|\mathbf{v}^{(k)} - \mathbf{v}^{(j)}\|_2^2 \right). \quad (80)$$

It follows from

$$\Delta_{k+1} = \frac{1}{\sqrt{nB}} \left( \|\mathbf{x}^{(k+1)} - \mathbf{x}^{(k)}\|_2 + \|\mathbf{v}^{(k+1)} - \mathbf{v}^{(k)}\|_2 \right). \quad (81)$$

that  $\Delta_{k+1} = D(\boldsymbol{\theta}^{(k+1)}, \boldsymbol{\theta}^{(k)})$ . If we can show that  $\{\boldsymbol{\theta}^{(k)}\}_{k=1}^\infty$  is a Cauchy sequence in  $\Theta$  with the distance function  $D$ , then  $\boldsymbol{\theta}^{(k)}$  should converge.

Now we consider the following two cases of updating  $\lambda_k$ :

- a) Monotone update rule by setting  $\lambda_{k+1} = \xi \lambda_k$ , with  $\xi < 1$  for all  $k$ .

In this case, it is easily to see from Eq. (75) and Eq. (79) that

$$\|\boldsymbol{\theta}^{(k+1)} - \boldsymbol{\theta}^{(k)}\|_2^2 \leq \left(7nBC - \frac{3nBCR_{\min}}{R_{\max}}\right) \lambda_0 \xi^{k-1} \quad (82)$$

$$\stackrel{0 < R_{\min} \leq R_{\max}}{\leq} 7nBC \lambda_0 \xi^{k-1}. \quad (83)$$

As  $\xi < 1$ , when  $k \rightarrow \infty$ ,  $\|\boldsymbol{\theta}^{(k+1)} - \boldsymbol{\theta}^{(k)}\|_2 \rightarrow 0$ . In other words,  $\{\boldsymbol{\theta}^{(k)}\}_{k=1}^{\infty}$  is a Cauchy sequence and therefore, there must exists  $\boldsymbol{\theta}^*$  such that

$$D(\boldsymbol{\theta}^{(k)}, \boldsymbol{\theta}^*) \rightarrow 0. \quad (84)$$

Consequently, we have  $\|\mathbf{x}^{(k)} - \mathbf{x}^*\|_2^2 \rightarrow 0$  and  $\|\mathbf{v}^{(k)} - \mathbf{v}^*\|_2^2 \rightarrow 0$ .

This is fixed-point convergence.

- b) Adaptive update via

- i) If  $\Delta_{k+1} \geq \eta \Delta_k$ , then  $\lambda_{k+1} = \xi \lambda_k$ .
- ii) If  $\Delta_{k+1} < \eta \Delta_k$ , then  $\lambda_{k+1} = \lambda_k$ .

In both cases,  $\xi < 1$ .

At  $k^{th}$  iteration, we have

– Case i) holds, from Eq. (75) and Eq. (79), we have

$$D(\boldsymbol{\theta}^{(k+1)}, \boldsymbol{\theta}^{(k)}) \leq 7C \lambda_{k-1}. \quad (85)$$

– Case ii) holds, since  $\Delta_{k+1} = D(\boldsymbol{\theta}^{(k+1)}, \boldsymbol{\theta}^{(k)})$ ,

$$D(\boldsymbol{\theta}^{(k+1)}, \boldsymbol{\theta}^{(k)}) < \eta D(\boldsymbol{\theta}^{(k)}, \boldsymbol{\theta}^{(k-1)}). \quad (86)$$

As  $k \rightarrow \infty$ , one of the following situations will happen

- S1: Case i) occurs infinite times but Case ii) occurs finite times.
- S2: Case ii) occurs infinite times but Case i) occurs finite times.
- S3: Both Case i) and Case ii) occur infinite times.

When S1 happens, there must exists a  $K_1$  such that for  $k \geq K_1$  only case i) will be visited. Following this,

$$D(\boldsymbol{\theta}^{(k+1)}, \boldsymbol{\theta}^{(k)}) \leq 7C \lambda_{K_1-1} \xi^{k-K_1-1}, \quad \forall k \geq K_1. \quad (87)$$

When S2 happens, there must exists a  $K_2$  such that for  $k \geq K_2$  only case ii) will be visited. Following this,

$$\begin{aligned} D(\boldsymbol{\theta}^{(k+1)}, \boldsymbol{\theta}^{(k)}) &< \eta^{k-K_2} D(\boldsymbol{\theta}^{(K_2)}, \boldsymbol{\theta}^{(K_2-1)}) \quad (88) \\ &\leq 7C \lambda_{K_2-2} \eta^{k-K_2}, \quad \forall k \geq K_2. \quad (89) \end{aligned}$$

Combing (87) and (89), we have, for any  $k \geq \max\{K_1, K_2\}$ ,

$$\begin{aligned} D(\boldsymbol{\theta}^{(k+1)}, \boldsymbol{\theta}^{(k)}) &\leq 7C \max\{\lambda_{K_1-1} \xi^{-K_1-1}, \lambda_{K_2-2} \eta^{-K_2}\} (\max\{\xi, \eta\})^k \quad (90) \end{aligned}$$

Let  $\tilde{C} = 7C \max\{\lambda_{K_1-1} \xi^{-K_1-1}, \lambda_{K_2-2} \eta^{-K_2}\}$  and  $\delta = \max\{\xi, \eta\}$ , we have

$$D(\boldsymbol{\theta}^{(k+1)}, \boldsymbol{\theta}^{(k)}) \leq \tilde{C} \delta^k, \quad (91)$$

for some constant  $\tilde{C}$  and  $\delta < 1$ .

Since S3 is a union of S1 and S2, we can verify that no matter which one of S1 to S3, for all integers  $m > k$  and  $k \rightarrow \infty$ ,

$$D(\boldsymbol{\theta}^{(m)}, \boldsymbol{\theta}^{(k)}) \rightarrow 0. \quad (92)$$

Following this,  $\{\boldsymbol{\theta}^{(k)}\}_{k=1}^{\infty}$  is a Cauchy sequence and thus it always converges. Therefore, there must exists  $\boldsymbol{\theta}^*$  such that

$$D(\boldsymbol{\theta}^{(k)}, \boldsymbol{\theta}^*) \rightarrow 0. \quad (93)$$

Consequently, we have  $\|\mathbf{x}^{(k)} - \mathbf{x}^*\|_2 \rightarrow 0$  and  $\|\mathbf{v}^{(k)} - \mathbf{v}^*\|_2 \rightarrow 0$ . □

## C. Proof of Theorem 2: Global Convergence of Plug-and-Play GAP

*Proof.* Again, let us start from (65), we have

$$\mathbf{x}^{(k+1)} - \mathbf{x}^* = \mathbf{v}^{(k)} - \mathbf{x}^* + \mathbf{H}^\top (\mathbf{H} \mathbf{H}^\top)^{-1} (\mathbf{y} - \mathbf{H} \mathbf{v}^{(k)}) \quad (94)$$

$$= \mathbf{v}^{(k)} - \mathbf{x}^* + \mathbf{H}^\top (\mathbf{H} \mathbf{H}^\top)^{-1} \mathbf{H} (\mathbf{x}^* - \mathbf{v}^{(k)}) \quad (95)$$

Following the derivation in (70), we have

$$\|\mathbf{x}^{(k+1)} - \mathbf{x}^*\|_2^2 = \|\mathbf{v}^{(k)} - \mathbf{x}^*\|_2^2 - \|\mathbf{R}^{-\frac{1}{2}} \mathbf{H} (\mathbf{v}^{(k)} - \mathbf{x}^*)\|_2^2 \quad (96)$$

$$\leq \left(1 - \frac{R_{\min}}{R_{\max}}\right) \|\mathbf{v}^{(k)} - \mathbf{x}^*\|_2^2. \quad (97)$$

This is

$$\begin{aligned} & \| \mathbf{x}^{(k+1)} - \mathbf{x}^* \|_2 \\ & \leq \sqrt{1 - \frac{R_{\min}}{R_{\max}}} \| \mathbf{v}^{(k)} - \mathbf{x}^* \|_2 \end{aligned} \quad (98)$$

$$\leq \sqrt{1 - \frac{R_{\min}}{R_{\max}}} \left( \| \mathbf{v}^{(k)} - \mathbf{x}^{(k)} \|_2 + \| \mathbf{x}^{(k)} - \mathbf{x}^* \|_2 \right) \quad (99)$$

$$\begin{aligned} & \leq \sqrt{1 - \frac{R_{\min}}{R_{\max}}} \| \mathbf{x}^{(k)} - \mathbf{x}^* \|_2 \\ & \quad + \sqrt{nBC\sigma_{k-1}(1 - \frac{R_{\min}}{R_{\max}})} \end{aligned} \quad (100)$$

$$\begin{aligned} & = \sqrt{1 - \frac{R_{\min}}{R_{\max}}} \| \mathbf{x}^{(k)} - \mathbf{x}^* \|_2 \\ & \quad + \sqrt{nBC(1 - \frac{R_{\min}}{R_{\max}})} \lambda_{k-1}^{\frac{1}{4}} \end{aligned} \quad (101)$$

$$\begin{aligned} & = \sqrt{1 - \frac{R_{\min}}{R_{\max}}} \| \mathbf{x}^{(k)} - \mathbf{x}^* \|_2 \\ & \quad + \lambda_0 \sqrt{nBC(1 - \frac{R_{\min}}{R_{\max}})} \xi^{\frac{k-1}{4}} \end{aligned} \quad (102)$$

Note that since  $\sqrt{1 - \frac{R_{\min}}{R_{\max}}} < 1$  and  $\xi < 1$  and therefore, when  $k \rightarrow \infty$ ,

$$\lambda_0 \sqrt{nBC(1 - \frac{R_{\min}}{R_{\max}})} \xi^{\frac{k-1}{4}} \rightarrow 0. \quad (103)$$

In the main result, we have defined

$$C_g = \lambda_0 \sqrt{nBC(1 - \frac{R_{\min}}{R_{\max}})} \xi^{-\frac{1}{4}}, \quad (104)$$

$$\varphi = \xi^{\frac{1}{4}}. \quad (105)$$

□

## D. Simulation and Reconstruction Details

**Benchmark data** We follow the simulation setup and use all the four benchmark datasets, *i.e.*, Kobe, Traffic, Runner, and Drop in [22]. We use two more datasets, *i.e.*, Crash and Aerial in [26]<sup>3</sup> to cover a wider range of scenes. Full comparison of reconstruction frames of all seven PnP-GAP algorithms listed in Table 1 is shown in Fig. 8.

It can be seen clearly that PnP-FFDNet provides overall comparable results as the state-of-the-art (best among all the seven methods listed here) method DeSCI, as shown in Fig. 8 with significantly reduced running time (3 seconds vs. 103 minutes), as shown in Table 1 in the main paper.

<sup>3</sup>The results of DeSCI (GAP-WNNM) is different from those reported in [26] because of parameter settings of DeSCI, specifically the input estimated noise levels for each iteration stage. We use exactly the same parameters as the DeSCI paper [22], which is publicly available at <https://github.com/liuyang12/DeSCI>.

**Large-scale data** Similar to the benchmark data, we simulate the color video SCI measurements for large-scale data with four YouTube slow-motion videos, *i.e.*, Messi<sup>4</sup>, Hummingbird<sup>5</sup>, Swinger<sup>6</sup>, and Football<sup>7</sup>.

The color video SCI system and sensing process follows the color video and depth SCI system in [61]. The schematic of a color video SCI system is shown in Fig. 9. A sequence of color scene is coded by the corresponding shifted random binary masks at each time step and finally summed up to form a snapshot measurement on the color Bayer RGB sensor (with a “RGGB” Bayer color filter array here).

For reconstruction, the snapshot measurement is split into four “RGGB” sub-measurements according to the Bayer pattern. These sub-measurements are reconstructed measurement-by-measurement following the gray-scale reconstruction process by iteratively update the signal in data domain (using GAP or ADMM) and prior domain (using plug-and-play denoisers). Finally, the reconstructed sub-video-frames representing different color channels (R, G1, G2, and B) are recombined to a mosaic image and then demosaiced to form full-color video frames. Note that for simulation of large-scale data using YouTube videos, we do not have the access to the raw video data before demosaicing, so we simply “up-sample” it by putting each color channel as the mosaic R, G1, G2, and B channels. In this way, there are two identical G channels here and the reconstructed and the size of demosaiced image is doubled (both in width and height). For example, for UHD color video Football with original image size of  $3840 \times 1644$ , the reconstructed video frames have the size of  $7680 \times 3288$  (demosaiced). To make the readers less confusing, we simply call it UHD here (8K UHD exactly). And the quantitative metrics (PSNR and SSIM) are calculated before demosaicing.

*We again strongly encourage the readers to watch the supplementary videos of the reconstructed large-scale video data.*

- largescale\_messi24.avi: A  $1920 \times 1080 \times 24$  video reconstructed from a snapshot.
- largescale\_hummingbird40.avi: A  $1920 \times 1080 \times 40$  video reconstructed from a snapshot.
- largescale\_swinger20.avi: A  $3840 \times 2160 \times 20$  video reconstructed from a snapshot.
- largescale\_football48.avi: A  $3840 \times 1644 \times 48$  video reconstructed from a snapshot.

<sup>4</sup><https://www.youtube.com/watch?v=sbPrev56Pd4>

<sup>5</sup>[https://www.youtube.com/watch?v=RtUQ\\_pz5wlo](https://www.youtube.com/watch?v=RtUQ_pz5wlo)

<sup>6</sup><https://www.youtube.com/watch?v=cfnbyX9G5Rk>

<sup>7</sup><https://www.youtube.com/watch?v=EGAuWZYe2No>

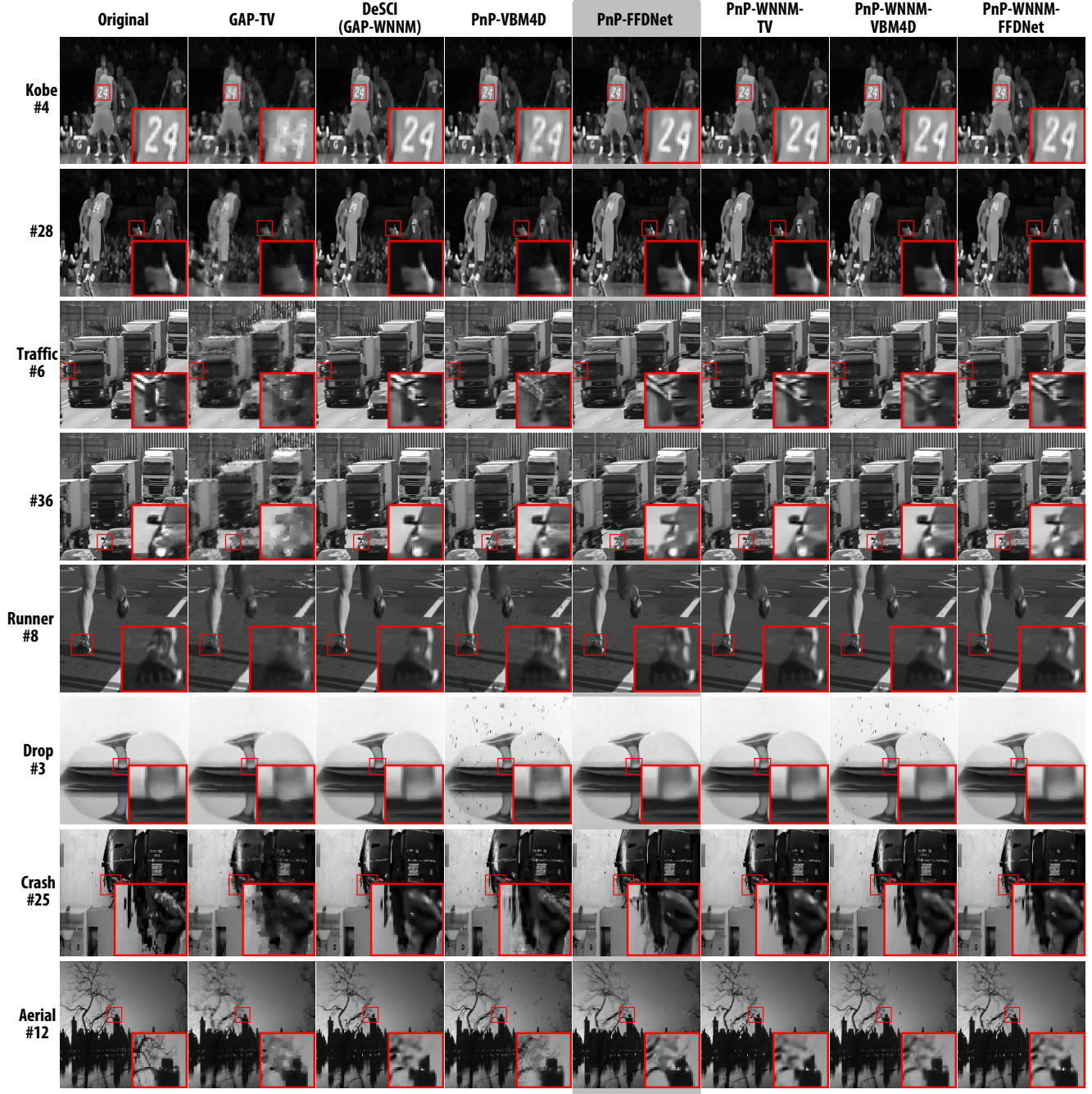


Figure 8. Full comparison of reconstructed frames of PnP-GAP algorithms (GAP-TV, DeSCI (GAP-WNNM), PnP-VBM4D, PnP-FFDNet, PnP-WNNM-TV, PnP-WNNM-VBM4D, and PnP-WNNM-FFDNet) on six simulated video SCI datasets.

**Performance varying compression ratios ( $B$ )** In order to further illustrate the efficiency of the proposed PnP algorithms for SCI, especially in real SCI systems varying compression ratios ( $B$ ), we show the reconstruction quality and speed of three PnP-SCI algorithms with compression ratios from 8 to 48 in Fig. 10 and Fig. 11, respectively. The data we used is the downsampled grayscale video of Football

with pixel resolution of 720p ( $1280 \times 720$ ). The other algorithms listed in Tab. 1 are too slow to be compared. And other deep-learning-based end-to-end networks, like [26, 34] would be not flexible to different compression ratios and require re-training the network for each compression ratio.

As we can see in Fig. 10 and Fig. 11, PnP-FFDNet is of the highest quality and fastest speed among these three

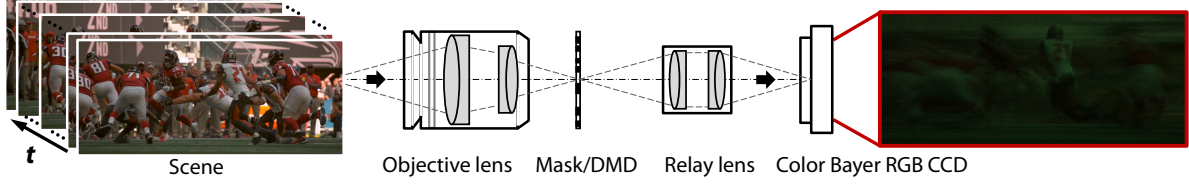


Figure 9. Schematic of a color video SCI system and its snapshot measurement (showing in Bayer RGB mode). A “RGGB” Bayer pattern is shown here.

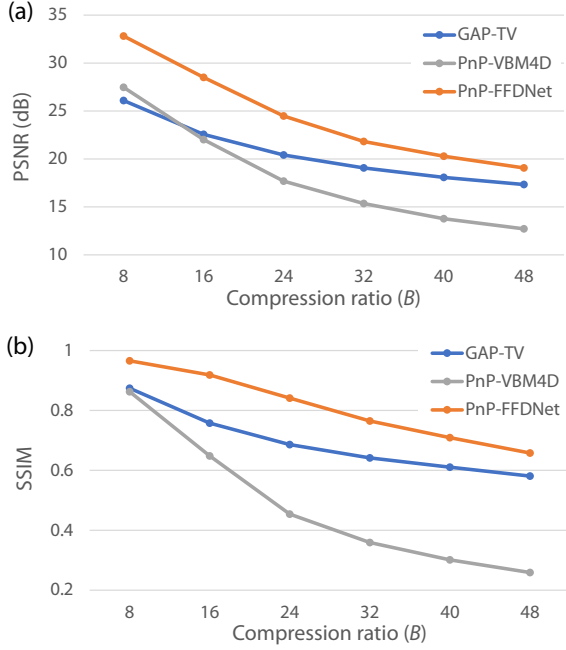


Figure 10. Reconstruction quality, *i.e.*, PSNR (a) and SSIM (b) varying compression ratios from 8 to 48. Higher is better.

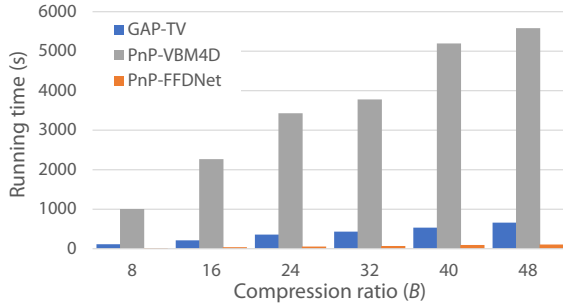


Figure 11. Running time (in seconds) varying compression ratios from 8 to 48. Lower is better.

fast PnP-SCI algorithms even with high compression ratios (up to 48). This further supports the idea that PnP-FFDNet would be the baseline for SCI reconstruction.

## E. More Experimental Results

We show additional experimental results of the proposed PnP framework of real data captured by SCI cameras here.

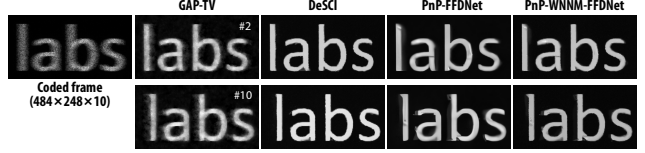


Figure 12. Real data: labs high-speed video SCI ( $484 \times 248 \times 10$ ).

As mentioned in Tab. 2 of the main paper, we show the results of labs [34] and UCF [40] in Fig. 12 and Fig. 13, respectively.

Similar to the observation of the main paper, from Fig. 12 and Fig. 13, we can see that PnP-FFDNet, which only takes about 12 seconds for reconstruction, can provide comparable results as DeSCI, which needs hours even when performed in a frame-wise manner, as shown in Tab. 2. And PnP-FFDNet is significantly better than the speed runner-up GAP-TV in terms of motion-blur reduction and detail preservation, as shown in Figs. 12 and 13. Note that PnP-FFDNet is more than  $5\times$  faster than GAP-TV in real datasets with regular size, and more than  $7\times$  faster in large-scale datasets. In this way, PnP algorithms for SCI achieves a good balance of efficiency and flexibility and PnP-FFDNet could serve as a baseline for SCI recovery.

## References

- [1] Yoann Altmann, Stephen McLaughlin, Miles J Padgett, Vivek K Goyal, Alfred O Hero, and Daniele Faccio. Quantum-inspired computational imaging. *Science*, 361(6403), 2018.
- [2] José M Bioucas-Dias and Mário AT Figueiredo. A new twist: Two-step iterative shrinkage/thresholding algorithms for image restoration. *IEEE Transactions on Image processing*, 16(12):2992–3004, 2007.
- [3] Stephen Boyd, Neal Parikh, Eric Chu, Borja Peleato, and Jonathan Eckstein. Distributed optimization and statistical learning via the alternating direction method of multipliers. *Foundations and Trends in Machine Learning*, 3(1):1–122, January 2011.
- [4] D. J. Brady, M. E. Gehm, R. A. Stack, D. L. Marks, D. S. Kittle, D. R. Golish, E. M. Vera, and S. D. Feller. Multiscale gigapixel photography. *Nature*, 486(7403):386–389, 2012.
- [5] David J. Brady, Alex Mrozack, Ken MacCabe, and Patrick Llull. Compressive tomography. *Advances in Optics and Photonics*, 7(4):756, 2015.
- [6] David J. Brady, Wubin Pang, Han Li, Zhan Ma, Yue Tao, and Xun Cao. Parallel cameras. *Optica*, 5(2), 2018.



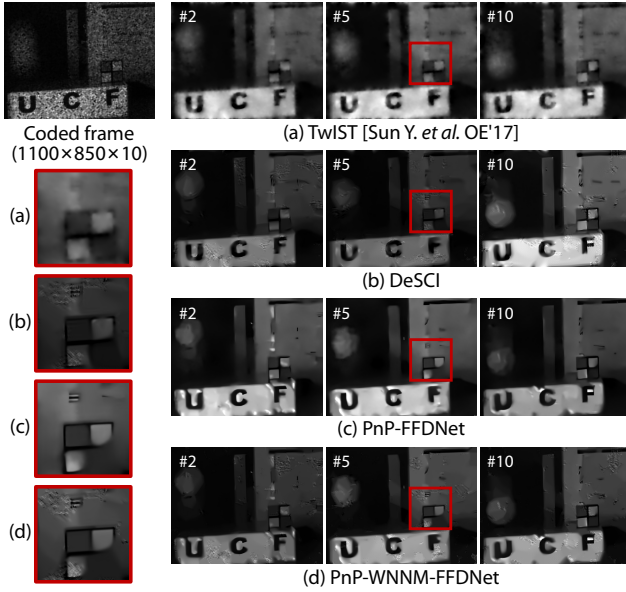


Figure 13. Real data: UCF high-speed video SCI ( $1100 \times 850 \times 10$ ).

- [7] E. Candés, J. Romberg, and T. Tao. Signal recovery from incomplete and inaccurate measurements. *Comm. Pure Appl. Math.*, 59(8):1207–1223, 2005.
- [8] Xun Cao, Tao Yue, Xing Lin, Stephen Lin, Xin Yuan, Qionghai Dai, Lawrence Carin, and David J Brady. Computational snapshot multispectral cameras: Toward dynamic capture of the spectral world. *IEEE Signal Processing Magazine*, 33(5):95–108, 2016.
- [9] Stanley H. Chan, Xiran Wang, and Omar A. Elgendy. Plug-and-play ADMM for image restoration: Fixed-point convergence and applications. *IEEE Transactions on Computational Imaging*, 3:84–98, 2017.
- [10] K. Dabov, A. Foi, V. Katkovnik, and K. Egiazarian. Image denoising by sparse 3d transform-domain collaborative filtering. *IEEE Transactions on Image Processing*, 16(8):2080–2095, August 2007.
- [11] David L Donoho et al. Compressed sensing. *IEEE Transactions on information theory*, 52(4):1289–1306, 2006.
- [12] M. E. Gehm, R. John, D. J. Brady, R. M. Willett, and T. J. Schulz. Single-shot compressive spectral imaging with a dual-disperser architecture. *Optics Express*, 15(21):14013–14027, 2007.
- [13] Shuhang Gu, Qi Xie, Deyu Meng, Wangmeng Zuo, Xiangchu Feng, and Lei Zhang. Weighted nuclear norm minimization and its applications to low level vision. *International Journal of Computer Vision*, 121(2):183–208, 2017.
- [14] Shuhang Gu, Lei Zhang, Wangmeng Zuo, and Xiangchu Feng. Weighted nuclear norm minimization with application to image denoising. In *IEEE Conference on Computer Vision and Pattern Recognition (CVPR)*, pages 2862–2869, 2014.
- [15] Yasunobu Hitomi, Jinwei Gu, Mohit Gupta, Tomoo Mitsunaga, and Shree K Nayar. Video from a single coded exposure photograph using a learned over-complete dictionary. In *2011 International Conference on Computer Vision*, pages 287–294. IEEE, 2011.
- [16] Michael Iliadis, Leonidas Spinoulas, and Aggelos K. Katsaggelos. Deep fully-connected networks for video compressive sensing. *Digital Signal Processing*, 72:9–18, 2018.
- [17] Shirin Jalali and Xin Yuan. Compressive imaging via one-shot measurements. In *IEEE International Symposium on Information Theory (ISIT)*, 2018.
- [18] Shirin Jalali and Xin Yuan. Snapshot compressed sensing: Performance bounds and algorithms. *IEEE Transactions on Information Theory*, 65(12):8005–8024, Dec 2019.
- [19] Kyong Hwan Jin, Michael T McCann, Emmanuel Froustey, and Michael Unser. Deep convolutional neural network for inverse problems in imaging. *IEEE Transactions on Image Processing*, 26(9):4509–4522, Sept 2017.
- [20] Kuldeep Kulkarni, Suhas Lohit, Pavan Turaga, Ronan Keriviche, and Amit Ashok. Reconnet: Non-iterative reconstruction of images from compressively sensed random measurements. In *CVPR*, 2016.
- [21] X. Liao, H. Li, and L. Carin. Generalized alternating projection for weighted- $\ell_{2,1}$  minimization with applications to model-based compressive sensing. *SIAM Journal on Imaging Sciences*, 7(2):797–823, 2014.
- [22] Yang Liu, Xin Yuan, Jinli Suo, David Brady, and Qionghai Dai. Rank minimization for snapshot compressive imaging. *IEEE Transactions on Pattern Analysis and Machine Intelligence*, 41(12):2990–3006, Dec 2019.
- [23] Patrick Llull, Xuejun Liao, Xin Yuan, Jianbo Yang, David Kittle, Lawrence Carin, Guillermo Sapiro, and David J Brady. Coded aperture compressive temporal imaging. *Optics Express*, 21(9):10526–10545, 2013.
- [24] Patrick Llull, Xin Yuan, Lawrence Carin, and David J Brady. Image translation for single-shot focal tomography. *Optica*, 2(9):822–825, 2015.
- [25] P. Llull, X. Yuan, X. Liao, J. Yang, D. Kittle, L. Carin, G. Sapiro, and D. J. Brady. *Compressed Sensing and its Applications: MATHEON Workshop 2013*, chapter Temporal Compressive Sensing for Video, pages 41–74. Springer International Publishing, 2015.
- [26] Jiawei Ma, Xiaoyang Liu, Zheng Shou, and Xin Yuan. Deep tensor admm-net for snapshot compressive imaging. In *IEEE/CVF Conference on Computer Vision (ICCV)*, 2019.
- [27] M. Maggioni, G. Boracchi, A. Foi, and K. O. Egiazarian. Video denoising, deblocking, and enhancement through separable 4-d nonlocal spatiotemporal transforms. *IEEE Transactions on Image Processing*, 21:3952–3966, 2012.
- [28] Xin Miao, Xin Yuan, Yunchen Pu, and Vassilis Athitsos.  $\lambda$ -net: Reconstruct hyperspectral images from a snapshot measurement. In *IEEE/CVF Conference on Computer Vision (ICCV)*, 2019.
- [29] Xin Miao, Xin Yuan, and Paul Wilford. Deep learning for compressive spectral imaging. In *Digital Holography and Three-Dimensional Imaging 2019*, page M3B.3. Optical Society of America, 2019.
- [30] Ali Mousavi and Richard G Baraniuk. Learning to invert: Signal recovery via deep convolutional networks. In *2017 IEEE International Conference on Acoustics, Speech and Signal Processing (ICASSP)*, pages 2272–2276, March 2017.
- [31] Joseph N. Mait, Gary W. Euliss, and Ravindra A. Athale. Computational imaging. *Adv. Opt. Photon.*, 10(2):409–483, Jun 2018.

- [32] Wei Ouyang, Andrey I. Aristov, Mickaël Lelek, Xian Feng Hao, and Christophe Zimmer. Deep learning massively accelerates super-resolution localization microscopy. *Nature Biotechnology*, 36:460–468, 2018.
- [33] Mu Qiao, Xuan Liu, and Xin Yuan. Snapshot spatial-temporal compressive imaging. *Opt. Lett.*, 2020.
- [34] Mu Qiao, Ziyi Meng, Jiawei Ma, and Xin Yuan. Deep learning for video compressive sensing. *APL Photonics*, 5(3):030801, 2020.
- [35] Mu Qiao, Yangyang Sun, Xuan Liu, Xin Yuan, and Paul Wilford. Snapshot optical coherence tomography. In *Digital Holography and Three-Dimensional Imaging 2019*, page W4B.3. Optical Society of America, 2019.
- [36] Dikpal Reddy, Ashok Veeraraghavan, and Rama Chellappa. P2C2: Programmable pixel compressive camera for high speed imaging. In *IEEE Conference on Computer Vision and Pattern Recognition (CVPR)*, pages 329–336.
- [37] Francesco Renna, Liming Wang, Xin Yuan, Jianbo Yang, Galen Reeves, Robert Calderbank, Lawrence Carin, and Miguel RD Rodrigues. Classification and reconstruction of high-dimensional signals from low-dimensional features in the presence of side information. *IEEE Transactions on Information Theory*, 62(11):6459–6492, Nov 2016.
- [38] Ernest K. Ryu, Jialin Liu, Sicheng Wang, Xiaohan Chen, Zhangyang Wang, and Wotao Yin. Plug-and-play methods provably converge with properly trained denoisers. In *ICML*, 2019.
- [39] Ayan Sinha, Justin Lee, Shuai Li, and George Barbastathis. Lensless computational imaging through deep learning. *Optica*, 4(9):1117–1125, Sep 2017.
- [40] Yangyang Sun, Xin Yuan, and Shuo Pang. High-speed compressive range imaging based on active illumination. *Optics Express*, 24(20):22836–22846, Oct 2016.
- [41] Yangyang Sun, Xin Yuan, and Shuo Pang. Compressive high-speed stereo imaging. *Opt Express*, 25(15):18182–18190, 2017.
- [42] T.H. Tsai, P. Llull, X. Yuan, L. Carin, and D.J. Brady. Coded aperture compressive spectral-temporal imaging. In *Computational Optical Sensing and Imaging (COSI)*, pages 1–3, 2015.
- [43] Tsung-Han Tsai, Patrick Llull, Xin Yuan, Lawrence Carin, and David J Brady. Spectral-temporal compressive imaging. *Optics Letters*, 40(17):4054–4057, Sep 2015.
- [44] Tsung-Han Tsai, Xin Yuan, and David J Brady. Spatial light modulator based color polarization imaging. *Optics Express*, 23(9):11912–11926, May 2015.
- [45] Ashwin Wagadarikar, Renu John, Rebecca Willett, and David Brady. Single disperser design for coded aperture snapshot spectral imaging. *Applied Optics*, 47(10):B44–B51, 2008.
- [46] Ashwin A Wagadarikar, Nikos P Pitsianis, Xiaobai Sun, and David J Brady. Video rate spectral imaging using a coded aperture snapshot spectral imager. *Optics Express*, 17(8):6368–6388, 2009.
- [47] Zhou Wang, Alan C Bovik, Hamid R Sheikh, Eero P Simoncelli, et al. Image quality assessment: From error visibility to structural similarity. *IEEE Transactions on Image Processing*, 13(4):600–612, 2004.
- [48] Junyuan Xie, Linli Xu, and Enhong Chen. Image denoising and inpainting with deep neural networks. In F. Pereira, C. J. C. Burges, L. Bottou, and K. Q. Weinberger, editors, *Advances in Neural Information Processing Systems 25*, pages 341–349. Curran Associates, Inc., 2012.
- [49] Jianbo Yang, Xuejun Liao, Xin Yuan, Patrick Llull, David J Brady, Guillermo Sapiro, and Lawrence Carin. Compressive sensing by learning a Gaussian mixture model from measurements. *IEEE Transaction on Image Processing*, 24(1):106–119, January 2015.
- [50] J. Yang, X. Yuan, X. Liao, P. Llull, G. Sapiro, D. J. Brady, and L. Carin. Video compressive sensing using Gaussian mixture models. *IEEE Transaction on Image Processing*, 23(11):4863–4878, November 2014.
- [51] Michitaka Yoshida, Akihiko Torii, Masatoshi Okutomi, Kenta Endo, Yukinobu Sugiyama, Rin-ichiro Taniguchi, and Hajime Nagahara. Joint optimization for compressive video sensing and reconstruction under hardware constraints. In *The European Conference on Computer Vision (ECCV)*, September 2018.
- [52] Xin Yuan. Compressive dynamic range imaging via Bayesian shrinkage dictionary learning. *Optical Engineering*, 55(12):123110, 2016.
- [53] Xin Yuan. Generalized alternating projection based total variation minimization for compressive sensing. In *2016 IEEE International Conference on Image Processing (ICIP)*, pages 2539–2543, Sept 2016.
- [54] Xin Yuan. Adaptive step-size iterative algorithm for sparse signal recovery. *Signal Processing*, 152:273–285, 2018.
- [55] Xin Yuan, David Brady, and Aggelos K. Katsaggelos. Snapshot compressive imaging: Theory, algorithms and applications. *IEEE Signal Processing Magazine*, 2020.
- [56] X. Yuan and R. Haimi-Cohen. Image compression based on compressive sensing: End-to-end comparison with jpeg. *IEEE Transactions on Multimedia*, pages 1–1, 2020.
- [57] X. Yuan, H. Jiang, G. Huang, and P. Wilford. Compressive sensing via low-rank Gaussian mixture models. *arXiv:1508.06901*, 2015.
- [58] X. Yuan, H. Jiang, G. Huang, and P. Wilford. SLOPE: Shrinkage of local overlapping patches estimator for lensless compressive imaging. *IEEE Sensors Journal*, 16(22):8091–8102, November 2016.
- [59] Xin Yuan, Xuejun Liao, Patrick Llull, David Brady, and Lawrence Carin. Efficient patch-based approach for compressive depth imaging. *Applied Optics*, 55(27):7556–7564, Sep 2016.
- [60] Xin Yuan, Patrick Llull, David J Brady, and Lawrence Carin. Tree-structure bayesian compressive sensing for video. *arXiv:1410.3080*, 2014.
- [61] Xin Yuan, Patrick Llull, Xuejun Liao, Jianbo Yang, David J. Brady, Guillermo Sapiro, and Lawrence Carin. Low-cost compressive sensing for color video and depth. In *IEEE Conference on Computer Vision and Pattern Recognition (CVPR)*, pages 3318–3325, 2014.
- [62] Xin Yuan and Shuo Pang. Compressive video microscope via structured illumination. In *2016 IEEE International Conference on Image Processing (ICIP)*, pages 1589–1593, Sept 2016.
- [63] Xin Yuan and Shuo Pang. Structured illumination temporal compressive microscopy. *Biomedical Optics Express*, 7:746–758, 2016.

- [64] X. Yuan and Y. Pu. Convolutional factor analysis inspired compressive sensing. In *2017 IEEE International Conference on Image Processing (ICIP)*, pages 550–554, Sept 2017.
- [65] Xin Yuan and Yunchen Pu. Parallel lensless compressive imaging via deep convolutional neural networks. *Optics Express*, 26(2):1962–1977, Jan 2018.
- [66] X. Yuan, V. Rao, S. Han, and L. Carin. Hierarchical infinite divisibility for multiscale shrinkage. *IEEE Transactions on Signal Processing*, 62(17):4363–4374, Sep. 1 2014.
- [67] Xin Yuan, Yangyang Sun, and Shuo Pang. Compressive temporal stereo-vision imaging. In *Computational Optical Sensing and Imaging (COSI)*, 2016.
- [68] Xin Yuan, Yangyang Sun, and Shuo Pang. Compressive temporal rgb-d imaging. In *Imaging and Applied Optics 2017 (3D, AIO, COSI, IS, MATH, pcAOP)*, page CTh1B.3. Optical Society of America, 2017.
- [69] X. Yuan, Y. Sun, and S. Pang. Compressive video sensing with side information. *Appl. Opt.*, 56(10):2697–2704, 2017.
- [70] Xin Yuan, Tsung-Han Tsai, Ruoyu Zhu, Patrick Llull, David Brady, and Lawrence Carin. Compressive hyperspectral imaging with side information. *IEEE Journal of Selected Topics in Signal Processing*, 9(6):964–976, September 2015.
- [71] Xin Yuan, Jianbo Yang, Patrick Llull, Xuejun Liao, Guillermo Sapiro, David J Brady, and Lawrence Carin. Adaptive temporal compressive sensing for video. *IEEE International Conference on Image Processing*, pages 1–4, 2013.
- [72] Z. Zha, X. Yuan, B. Wen, J. Zhou, J. Zhang, and C. Zhu. From rank estimation to rank approximation: Rank residual constraint for image restoration. *IEEE Transactions on Image Processing*, 29:3254–3269, 2020.
- [73] Zhiyuan Zha, Xinggan Zhang, Yuehua Wu, Qiong Wang, Xin Liu, Lan Tang, and Xin Yuan. Non-convex weighted p nuclear norm based admm framework for image restoration. *Neurocomputing*, 311:209–224, 2018.
- [74] Kai Zhang, Wangmeng Zuo, Yunjin Chen, Deyu Meng, and Lei Zhang. Beyond a Gaussian denoiser: Residual learning of deep CNN for image denoising. *IEEE Transactions on Image Processing*, 26(7):3142–3155, 2017.
- [75] Kai Zhang, Wangmeng Zuo, and Lei Zhang. FFDNet: Toward a fast and flexible solution for CNN-based image denoising. *IEEE Trans. Image Processing*, 27(9):4608–4622, 2018.
- [76] Xinyuan Zhang, Xin Yuan, and Lawrence Carin. Nonlocal low-rank tensor factor analysis for image restoration. In *IEEE Conference on Computer Vision and Pattern Recognition (CVPR)*, pages 3318–3325, 2018.